Bottom-effect in Atomic Force Microscopy Nanomechanics

Dr. Stefano Chiodini, Silvia Ruiz-Rincón[†], Dr. Pablo D. Garcia[†], Dr. Santiago Martin, Dr. Katharina Kettelhoit, Dr. Ilaria Armenia, Prof. Daniel B. Werz, Prof. Pilar Cea**

Dr. S. Chiodini, S. Ruiz-Rincón, Prof. P. Cea

Instituto de Nanociencia de Aragón (INA), Campus Rio Ebro, Universidad de Zaragoza, C/Mariano Esquillor s/n, 50018 Zaragoza, Spain

Email: schiodini@unizar.es, pilarcea@unizar.es

Dr. S. Chiodini, S. Ruiz-Rincón, Prof. P. Cea

Laboratorio de Microscopias Avanzadas (LMA), Campus Río Ebro, Universidad de Zaragoza, C/Mariano Esquillor s/n, 50018 Zaragoza, Spain

Dr. S. Chiodini, S. Ruiz-Rincón, Dr. S. Martin, Prof. P. Cea

Departamento de Química Física, Facultad de Ciencias, Universidad de Zaragoza, C/Pedro Cerbuna 12, 50009, Zaragoza, Spain

Dr. P. D. Garcia

Instituto de Ciencia de Materiales, ICMM-CSIC, Campus de Cantoblanco, C/Sor Juana Inés de la Cruz, 3, 28049, Madrid, Spain

Prof. P. Cea, Dr. S. Martin, Dr. I. Armenia

Instituto de Ciencia de Materiales de Aragón (ICMA), Universidad de Zaragoza-CSIC, C/Pedro Cerbuna 12, 50009, Zaragoza, Spain

Dr. K. Kettelhoit, Prof. D. B. Werz

TU Braunschweig, Institut für Organische Chemie, Hagenring 30, 38106, Braunschweig, Germany

*corresponding author

†These authors have equally contributed to this work

Keywords: mechanobiology, bottom-effect artefact, afm nanomechanics, afm force-spectroscopy, supported lipid membranes

In this contribution the influence of the rigid substrate on the determination of the sample Young modulus, the so called *bottom-effect artefact*, is demonstrated by an AFM force-spectroscopy experiment. The nanomechanical properties of a one component supported lipid membrane (SLM) exhibiting areas of two different thicknesses are studied: while a standard contact mechanics model (Sneddon) provides two different elastic moduli for these two morphologies, it is shown that Garcia's bottom-effect artefact correction yields a unique value, as expected for an intrinsic material property. Remarkably, it is demonstrated that the ratio between the contact radius (and not only the indentation) and the sample thickness is the key parameter addressing the relevance of the bottom-effect artefact. The experimental results are validated by finite element method (FEM) simulations providing a solid support to Garcia's theory. The amphiphilic nature of the investigated material is representative of several kinds of lipids, suggesting that our results have far reaching implications for determining the *correct* Young modulus of SLMs. The generality of Garcia's bottom-effect artefact correction allows its application to every kind of supported soft film.

1. Introduction

Mechanobiology aims to understand how biological systems sense, transduce and respond to mechanical cues and despite a century of history, represents today a crucial research line in the interdisciplinary fields of Nanoscience, Nanotechnology and Life Sciences.[1-2] In this context, mechanical properties have been recognized as an essential tool for characterizing soft biological matter, such as cells, tissues and membranes.[3-4] In the case of cells, a relationship between their elasticity and physiological and pathological state has been established.[5-7] Accordingly, extensive research has been carried out also on model cell membranes, *e.g.* Supported Lipid Membranes (SLMs), as manageable and relatively simple platforms that can be analyzed by different surface techniques.[8] SLMs are reasonably easy to obtain, present two-dimensional order, lateral mobility and they are a relevant tool for the study of lipid lateral interactions, formation of rafts, interactions between the lipid membrane and proteins, drugs, nanoparticles, ions, etc.[9-11]

Atomic Force Microscopy (AFM) has become an invaluable surface characterization technique for SLMs due to its high spatial,[12] force and time[13] resolutions achievable even in liquid environments at controlled temperatures. AFM imaging of soft mono and multilayered films has revealed either homogeneous or phase-separated morphologies,[14-16] accompanied by a comprehensive understanding of molecular interactions among the film components.[17-19] Molecular and sub-molecular resolution AFM images of lipid membranes have been obtained by several authors[20-22] and hydration layers at the water-lipid interface have been investigated by frequency modulation AFM.[23] Remarkably, AFM allows to go beyond imaging, providing mechanical material properties at the nanoscale.[24-31] Regarding SLMs, for instance, their nanomechanical properties can be investigated by AFM force-spectroscopy (AFM-

FS) “breakthrough experiments” where the (breakthrough) force required to rupture the membrane is measured. This force has been found to be directly related to the lateral interaction between lipid molecules,[32] hence it is regarded as the fingerprint of the mechanical stability of a SLM in a specific liquid environment.[33] Additionally, other relevant physical parameters can be extracted from breakthrough experiments including the sample Young modulus and the adhesion force.[34]

AFM-FS nanomechanical experiments rely on the acquisition of an array of deflection - displacement curves on the sample to obtain, by means of the calibrated deflection sensitivity and cantilever spring constant, a set of force-indentation curves. These are typically fitted with an appropriate contact mechanics model to obtain the (effective) Young modulus of the sample as a best-fit parameter. Several models have been proposed and, among them, Sneddon[35-36] and Hertz[37] approaches, are the most commonly used. While Sneddon’s theory tackles the general problem of any axisymmetric tip geometry (spherical, paraboloidal, conical…), the Hertz’s theory is more restricted, considering only the case of a paraboloidal tip shape. Remarkably, Hertz’s approach can be considered a very good approximation of a spherical tip in case of small indentations.[38] These two models are based on three main assumptions:[38] 1) a *continuum* sample, 2) linearity between stress and strain tensors and 3) an infinite sample thickness. While the first hypothesis means that the actual discrete (atomistic) nature of the sample does not affect the nanomechanical properties, the second one is crucial to relate the force-indentation curves only to the elastic property of the sample, ruling out any quadratic contribution. The third assumption, instead, considers that the rigid substrate, on which the sample is deposited, is too far from the indentation region to affect the nanomechanical properties of the sample. However, Dimitriadis and coworkers[39] have theoretically demonstrated that the contribution to the Young

modulus of the underlying rigid substrate is in general *not negligible*. Following a *naive* description, when the sample is indented with the AFM tip, the applied force propagates through the *finite* sample thickness until the rigid substrate and bounces back modifying the cantilever deflection. This adds an artefact to the Young modulus of the sample, resulting in an overestimation of the real value. Such effect is usually called the *bottom-effect artefact*.[40-41] Recently, Garcia *et al*.[41] extended the bottom-effect theory giving a more general description and providing finite element method (FEM) simulations. An extension of this phenomenon from elastic to viscoelastic samples was also published by the same authors.[42] However, despite several *theoretical* and *numerical* contributions,[39-44] direct *experimental* proofs of the bottom-effect artefact and of Garcia's approach validity are still scarce in literature.[45]

In this contribution, the existence of the bottom-effect artefact is experimentally demonstrated and the validity of Garcia's theory to determine the correct sample Young modulus, free of the substrate influence, is confirmed by AFM-FS experiments performed on a synthetic glycosphingolipid (GSL) SLM on mica. The GSL was deposited onto mica by the Langmuir-Schaefer (LS) technique resulting in a SLM mainly composed of 2-layers and 4-layer regions. These two regions modulate in two different ways the bottom-effect artefact allowing to probe, by AFM, a change in the SLM nanomechanical properties. By fitting the force-indentation curves with Sneddon's formula, indeed, two different Young moduli are obtained, depending on the indented film thickness. In contrast, when Garcia's formula with a 4^{th} order correction is used, a unique value for the sample Young modulus is obtained, restoring it as an intrinsic material property. Finally, FEM simulations are provided showing a good agreement with the experimental force-indentation curves, confirming once again the robustness of Garcia's bottom-effect theory.

2. Results and discussion

The chemical structure of the amphiphilic molecule used to prepare the SLM is shown in **Figure 1a**, while the corresponding synthetic protocol is fully reported in the Supporting Information (SI), Section 1.

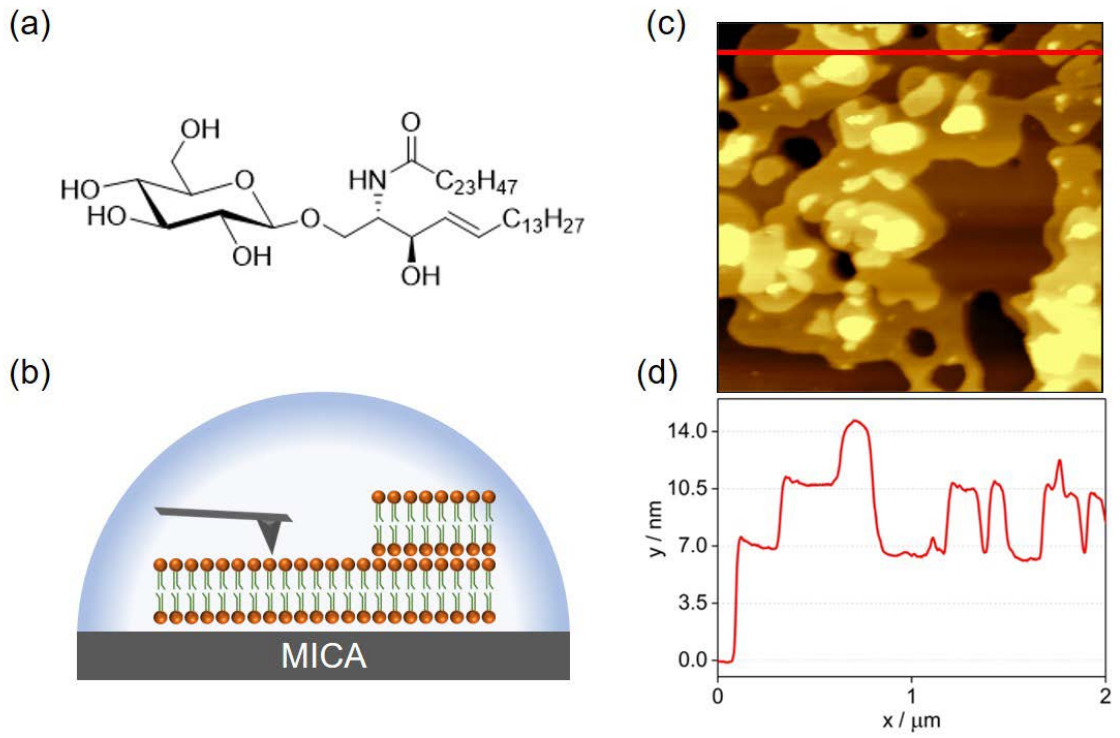

Figure 1. a) Chemical structure of the GSL molecule. b) Illustration of the AFM experiment in a liquid environment. The two main areas, 2-layer and 4-layer regions, of the GSL SLM can be distinguished. c) Representative AFM image of a 2 µm x 2 µm region of the GSL SLM in 10 mM HEPES, 300 mM NaCl, 20 mM $MgCl_2$ (pH = 7.4), on a mica substrate. d) Profile corresponding to the red line in Figure 1c. Three regions of *ca.* 7 nm, 11 nm and 14 nm in height can be distinguished, which can be ascribed to 2-layer, 3-layer and 4-layer regions, respectively.

This compound is a synthetic GSL with a β-D glucose as a polar head group that favors the anchoring of the molecules on the water subphase by the LS method; additionally, this GLS contains two hydrocarbon chains of different length that provide

insolubility in water and favor lateral van der Waals interactions between neighbor molecules that stabilize the Langmuir film. The length of this molecule, assuming a *trans zig-zag* configuration of the alkyl chains was calculated theoretically to be 3.3 nm using the program Spartan®08 V 1.0.0. This GSL was selected among a large catalogue of synthetic biomaterials in our laboratory due to its ability to form ordered films with regions of different thicknesses on the substrate (Figure 1b-c-d).

The SLM was deposited onto a mica substrate by the LS technique, where the substrate is horizontally approached (and then immediately withdrawn) to the water surface in a Langmuir trough containing a GSL monolayer (for further details see the SI, Section 2). As a result, a film exhibiting regions of different thickness was obtained (Figure 1b-c-d). In order to check that the polar heads of the GSL molecules are exposed to the liquid environment, the hydrophilicity of the film surface was tested by measurements of the contact angle of a drop of water. A value lower than 10° was obtained confirming a high hydrophilicity of the membrane surface (see the SI, Section 3).

Figure 1c shows an AFM image of the GSL SLM obtained in 10 mM HEPES, 300 mM NaCl and 20 mM $MgCl_2$ (pH = 7.4). This buffer was chosen on the one hand to mimic physiological conditions and on the other hand to expose the sample to a high ionic strength in order to reduce the extension of the tip-sample electrostatic interactions. From this image, three main regions with heights of *ca*. 7, 11 and 14 nm (Figures 1c-d) can be distinguished. Taking into account the GSL molecule maximum length (3.3 nm), the membrane regions whose thickness is *ca.* 7, 11 and 14 nm are consistent with 2-layer, 3-layer and 4-layer patches, respectively. The small difference (about half a nanometer) between the theoretical double of the molecule length (6.6 nm) and the bilayer thickness (*ca.* 7 nm) could be due to the presence of a thin liquid layer at

the mica interface, as reported in literature,[46-48] or eventually, to an apparent larger sample height caused by electrostatic interactions with the tip.[49] In the following, only 2-layer and 4-layer regions will be studied since these are the most relevant for a bottom-effect artefact proof based on different thickness morphologies of the *same* indented material (see later).

To study the nanomechanical properties of the described GSL SLM, an AFM-FS experiment was performed whose procedure is illustrated in **Figure 2a**.

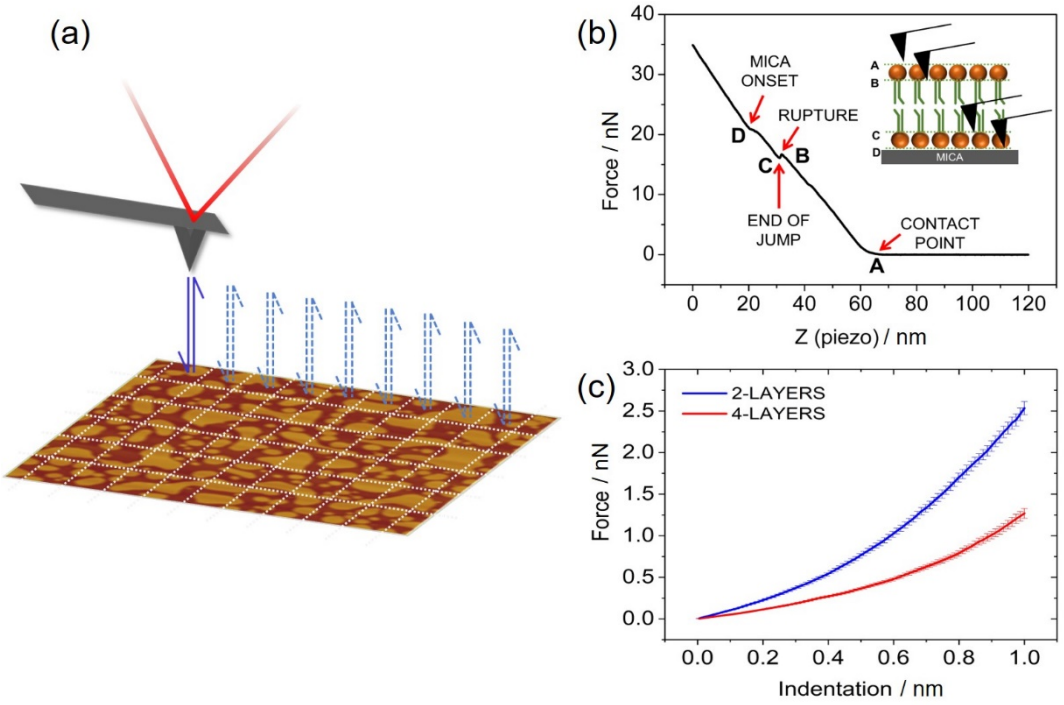

Figure 2. a) Representation of the AFM force-spectroscopy experiment where an array of force-distance curves is performed by approaching and withdrawing the cantilever onto the sample. b) Representative force-distance curve performed on the GSL SLM on mica in a liquid medium. The four main points, from A to D, are highlighted: point A is the contact point, point B provides the breakthrough force, point C the jump and point D the final contact with the mica substrate. c) Averaged force-indentation curves obtained from the raw experimental data. Blue data correspond to the average of ca. 180 curves of indentations on 2-layer regions (ca. 7 nm) whilst red data refer to ca. 60 curves onto 4-layer regions (ca. 14 nm).

After immersion of the sample in the liquid media, a 2 x 2 μm^2 AFM image was recorded. An array of *ca.* 20 x 20 force-distance curves onto the sample was performed by approaching and then withdrawing the cantilever to/from the sample in order to analyze its nanomechanical properties. A representative AFM (approach) force-distance curve obtained on a bilayer region in liquid is provided in Figure 2b (ten additional curves are provided in Figure S15 of the SI. All these curves show the same shape as the one in Figure 2b). The black line is the set of raw experimental data. Some points are especially noteworthy to describe the AFM-FS curve. Starting from far, *Z* (piezo) ≃ 120 nm, a region of no interaction is clearly visible, which corresponds to a negligible tip-sample force. At *Z* (piezo) ≃ 65 nm, the contact point is reached (point A), and the tip starts to indent the sample resulting in an increase of the recorded force. This increase lasts until the rupture event (point B) occurs, where a jump is visible in the force-distance curve; this event corresponds to the rupture of the GSL polar heads top layer at the solid-liquid interface and the consequent fall of the tip through the soft GSL hydrocarbon chains until the last polar heads in contact with mica are reached (points B-C). Then, the final indentation takes place till the mica is touched by the tip and the onset of the mica contact regime (with zero indentation) can be distinguished (point D). Notably, the *Z* (piezo) distance between point A and point D is *not* equal to the bilayer thickness, *ca.* 7 nm. This is due to the deflection of the cantilever during indentation. To restore the proper GSL bilayer thickness, indeed, a force – *indentation* plot should be considered.[50]

Once the force-distance curves were recorded, a customized Nanomechanics Python code (a full description of this code is provided in the SI, Section 5) was used to extract the sample Young modulus from the experimental force-indentation curves. In this code, a specific contact mechanics model must be selected, together with a proper

choice of the contact point (see SI, Section 5c).[51] As a first approximation, Sneddon's model for a paraboloidal tip geometry was applied:

$$F_{\mathrm{SNEDDON}} = \frac{4}{3} E_{eff} \sqrt{R} \delta^{3/2} \quad (1)$$

where E_{eff}, R and δ are the effective Young modulus, the tip radius and the indentation, respectively. More specifically, the effective Young modulus, E_{eff}, reads as:

$$\frac{1}{E_{eff}} = \frac{(1-\upsilon_t^2)}{E_t} + \frac{(1-\upsilon_s^2)}{E_s} \quad (2)$$

with υ_t, υ_s, E_t and E_s equal to the tip Poisson coefficient (υ_t = 0.3), the sample Poisson coefficient (υ_s = 0.5),[24] the tip Young modulus (E_t = 170 GPa) and the sample Young modulus, respectively.

Equation (1) relies on two additional assumptions: i) no adhesion between AFM tip and sample and ii) a paraboloidal tip geometry. For our experiments, the first hypothesis holds true, as can be seen in Figure S8 of the SI. Regarding the second assumption, a spherical geometry was initially assumed due to a nominal tip radius between 2 and 12 nm. Notably, in case of small indentations (smaller than the tip radius), the spherical tip geometry can be approximated by a paraboloidal one, a tip shape which will be considered throughout this contribution. Since Sneddon's model does not correct the bottom-effect artefact, it is expected to be sensible to the two thicknesses exhibited by the GSL SLM (Figure 1b), therefore providing two different sample Young modulus values despite the material being the same.

Recently, Garcia *et al.*[41] have proposed a complete correction to the bottom-effect artefact which, for the same paraboloidal tip geometry, yields the following force-indentation contact mechanics expression:

$$F_{\mathrm{GARCIA}} = F_{\mathrm{SNEDDON}}\left[1 + \frac{1.133\sqrt{\delta \mathrm{R}}}{h} + \frac{1.497\delta \mathrm{R}}{h^2} + \frac{1.469\delta \mathrm{R}\sqrt{\delta \mathrm{R}}}{h^3} + \frac{0.755(\delta \mathrm{R})^2}{h^4}\right] \quad (3)$$

As can be seen, this equation provides a correction to Sneddon's formula, made up of four terms. Remarkably, these terms are a function of the ratio between the contact radius, $(\delta \cdot R)^{1/2}$, and the thickness, *h*, of the indented membrane.

In Figure 2c, the *averaged* force-indentation curves conducted on 2-layer and 4-layer regions are reported, *i.e.* 7 nm (blue curve) and 14 nm (red curve) thick layers, respectively. Both curves were truncated at *ca.* 1 nm of maximum indentation in order to endorse the paraboloidal tip geometry assumption (as discussed above) and, at the same time, to avoid any kind of non-linearity (between stress and strain) related to the breakthrough force event (at *ca.* 20 nN, Figure 2b, point B-C and Figure S9 of the SI, Section 5b). To this maximum indentation corresponds a maximum strain (indentation/sample thickness) of *ca.* 14%, therefore less than what is considered the limit for a purely elastic sample, *i.e.* 20%.[3] Despite the material being the same, the two curves follow different behaviors, with the blue curve (2-layer regions) presenting higher force values, at the same indentation, with respect to the red curve (4-layer regions). We claim that this observation represents the fingerprint of the bottom-effect artefact, which is more pronounced on the 7 nm thick membrane due to a shorter distance from the mica rigid substrate. Basically, the presence of 2-layer and 4-layer regions of the same GSL material determines the magnitude of the bottom-effect artefact by changing the propagation length of the applied tip force, from the contact point (Figure 2b, point A), to the underneath mica substrate (Figure 2b, point D).

In **Figure 3** a more comprehensive analysis of the bottom-effect artefact is provided for the system under investigation (see panel a). The analysis of the force-indentation curves in order to determine the sample Young modulus, was performed by

means of the previously described Nanomechanics Python code where a paraboloidal tip geometry is assumed. Figure 3b shows the sample Young modulus histograms corresponding to force-indentation curves performed on 2-layer regions (blue data) and on 4-layer thick regions (red data).

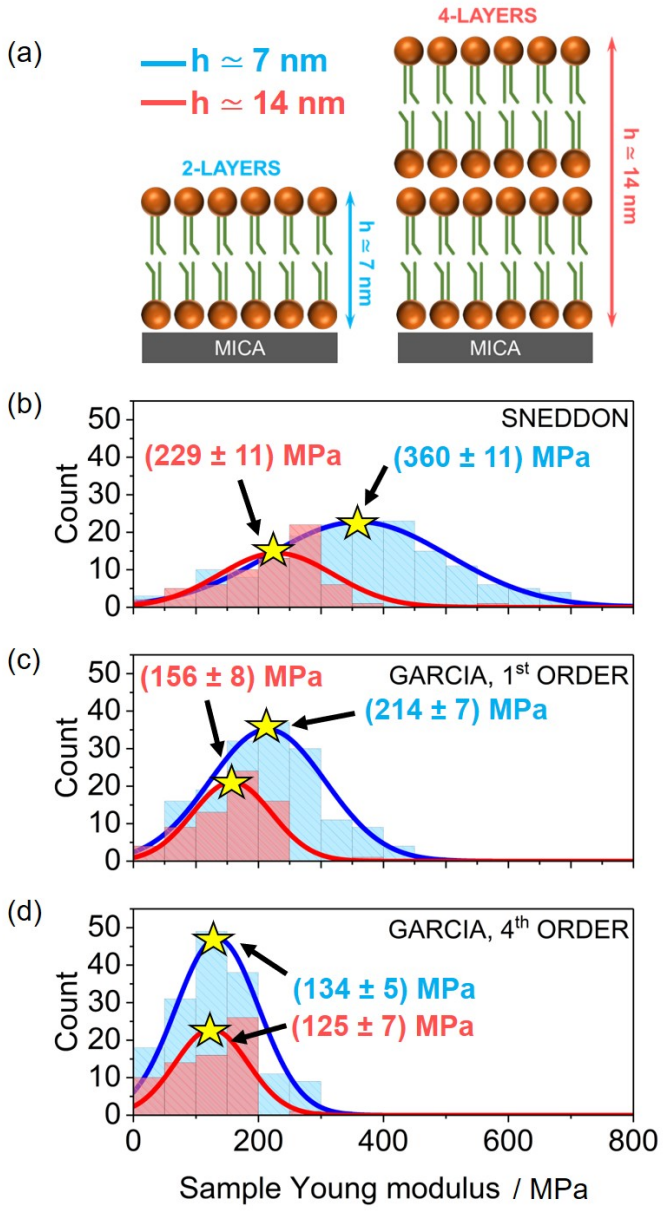

Figure 3. a) Scheme of the system under investigation made up of 2-layer regions (height h ≃ 7 nm) and 4-layer regions of GSL (height h ≃ 14 nm). b) Young modulus histogram obtained by force-distance curves performed on 2-layer (blue data) and 4-layer (red data) regions using Sneddon's formula, Equation (1). c) Young modulus histogram obtained by using Garcia's 1st order correction formula, Equation (3). d)

Young modulus histogram obtained with Garcia's 4th order correction formula, Equation (3). In Figure 3b-c-d the solid blue and red lines are Gaussian fittings of the 2-layer and 4-layer histograms, respectively, while the yellow stars indicate the histograms mean values. Main parameters used in the simulation (for more information refer to the SI or the AFM methods section): R = 17 nm, k = 0.6878 $N \cdot m^{-1}$, deflection sensitivity S = 14.46 $nm \cdot V^{-1}$, χ^2 = 10 (see the SI, Section 5f), geometry of the tip: paraboloidal. N (blue data) = 180, N (red data) = 60.

Fitting the force-indentation curves with Sneddon's theory, Equation (1), results in two clearly different Young moduli since the bottom-effect is not considered, which clearly evidences that the presence of the rigid substrate is not negligible. The difference in the Young modulus value for the 2-layer and 4-layer regions is (131 ± 16) MPa despite the same nature of the indented sample. Remarkably, the Young modulus obtained for 7 nm thick regions, is higher than the elastic modulus for a 14 nm thick area revealing the fingerprint of the bottom-effect artefact, more pronounced in the case of 2-layer regions. In contrast, fitting with Garcia's complete formula (at the 4th order correction), Equation (3), provides the *same* Young modulus value (within the error bars), *ca*. 130 MPa (Figure 3d) for the 2-layer and the 4-layer regions (Figure 3d). This result is in agreement with the elastic modulus as an intrinsic material property (therefore independent from the sample thickness) and it explicitly shows that the bottom-effect artefact is fully compensated by a 4th order correction of Garcia's formula. Additionally, this nanomechanical analysis was performed on 3-layer regions, *i.e. ca.* 11 nm thick patches, showing results in agreement with Figure 3 main trends (Section 5e in the SI).

The obtained Young modulus value for the GSL SLM (Figure 3b), is in good agreement with previously reported values for phospholipids molecules ranging from *ca.* 30 MPa to 300 MPa[21, 24, 27, 52] with eventual discrepancies attributable to

differences in the chemical structure of the biological material under investigation and to the presence of salts in the buffer.[21, 52]

The statistical analysis of the sample Young modulus, was also performed fitting all the force-indentation curves with Garcia's formula (Equation (3)) but using only the 1st order correction. As shown in Figure 3c, the bottom-effect artefact correction truncated at the 1st order, yields two closer values of elastic modulus with respect to the simple approach of Sneddon (here the difference is only 58 MPa) but still does not fully compensate the rigid substrate contribution to the sample Young modulus. For the 2nd and 3rd order Garcia's corrections differences of 17 MPa and 15 MPa are obtained, confirming a progressive correction coming from the four terms of Equation (3).

All these experimental results confirm that the use of Garcia's bottom-effect artefact correction is unavoidable for a *correct* determination of the elastic modulus of soft films supported on a rigid substrate, otherwise the accuracy of the Young modulus can be highly questionable.

To further test the validity of Figure 3 results, finite element method (FEM) simulations were performed (more details in the methods section); FEM simulations are considered to provide the correct nanomechanical behavior of the material under investigation and have already been demonstrated to be in agreement with Garcia's theory.[41] **Figure 4a** shows the interface between the vertical indenting AFM tip, not drawn for clarity, a finite elastic 2-layer region (thickness of 7 nm) and the rigid support. For a simulated maximum indentation of 1 nm, the Von Misses[53] stresses extend through the full thickness of the elastic layer, due to the relative wide contact radius. This propagation of the stress is the cause of the bottom-effect artefact, since it connects mechanically the tip and the substrate. In Figure 4b, the force-indentation

curves data obtained by FEM simulations (symbols) are compared with the averaged experimental data (solid line) obtaining a good agreement which also demonstrates the consistency of two of the physical hypotheses discussed in the introduction section: the continuous nature and the linearity of the sample. These two assumptions are explicitly included in the FEM model, but they do not necessarily hold for every material under study. However, the agreement between simulations and experimental results shown in Figure 4b, strongly support their validity.

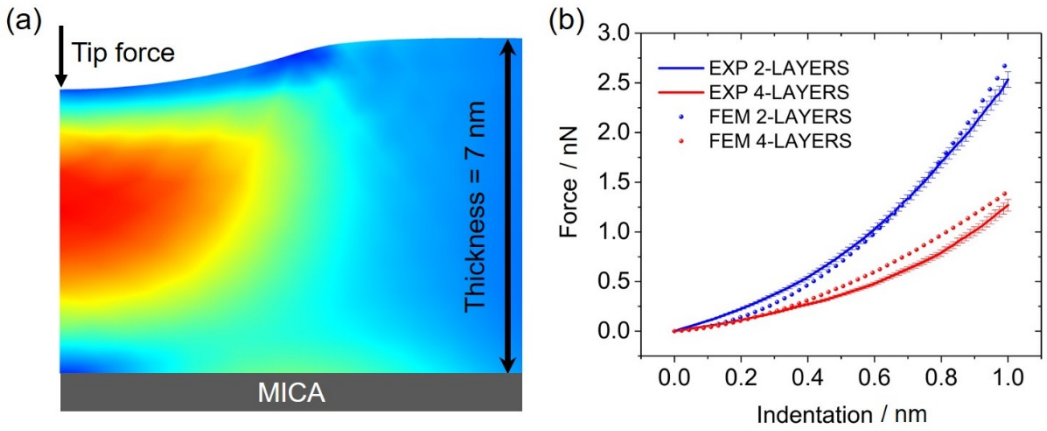

Figure 4. a) Cross section of a FEM simulation of the AFM tip indenting a 2-layer region (7 nm). The color map represents the simulated Von Misses stress inside the sample (red: high stress, blue: small stress), due to the vertical force applied by the spherical tip (not shown for clarity). b) Force-indentation curves comparison between FEM simulations (symbols) and averaged experimental data (solid lines), for the two different layer thicknesses (2-layers: blue data (*ca.* 180 curves), 4-layers: red data (*ca.* 60 curves)).

Nonetheless, a small discrepancy between experimental and FEM data is still present in Figure 4b, mainly in the 4-layers case (red data). This error could be due to several reasons: i) the FEM simulations do not take into account any viscosity of the sample since only elastic properties were considered. As already reported in literature, phospholipids do show viscoelastic behaviors[27, 54] therefore addressing the necessity for a more complete mechanical description, ii) the FEM simulations are based on

linear elasticity which, as well, could be only a first order description, neglecting non-linear contributions, iii) the 4-layers experimental curve (red solid line) corresponds to the average of *ca.* 60 force-indentation curves, *i.e.* a slightly poor statistics. This could also be a partial reason for a worse 4-layers fitting with respect to a 2-layers experimental curve which is related to a higher statistic, *ca.* 180 curves. As can be appreciated in Figure 1c, indeed, the coverage of 4-layers regions is smaller than the coverage of 2-layers areas.

Finally, following Equation (3), we stress that the ratio between the *contact radius*, $(\delta \cdot R)^{1/2}$, and the sample thickness *h*, is the key parameter for the evaluation of the relevance of the bottom-effect artefact for the AFM nanomechanical properties of a supported sample. In the example here studied, due to a maximum indentation of 1 nm and a tip radius of 17 nm (see the SI: Section 6 and also section 7 with SEM images of the tip), the ratio between the contact radius and the sample thickness is *ca.* 0.5, which fully addresses a relevant bottom-effect artefact. This conclusion is also supported by the simulation provided in Figure 4a, where the vertical dimension of the red region (high-stress zone) is in the same order of magnitude than the contact radius. As the stresses are a kind of mechanical connection between the tip and the sample, also this observation addresses a relevant bottom-effect artefact. Hence, these results indicate that the accepted rule - of a maximum indentation less than 10-20% of the sample thickness to be enough for a negligible bottom-effect artefact – cannot be generally applied.

3. Conclusions

This contribution provides an AFM force-spectroscopy experimental proof of the existence of the so-called bottom-effect artefact for the elastic Young modulus

determination of a supported lipid membrane. In particular, a glycosphingolipid sample exhibiting regions of different thicknesses onto a rigid mica substrate was obtained by the Langmuir-Schaefer technique and its mechanical properties analysed. The application of a standard contact mechanics model such as Sneddon's theory, yields a thickness dependent value for the Young modulus due to a modulation of the bottom-effect artefact by the varying thickness of the sample. Remarkably, the results here provided strongly support the validity of Garcia's correction to the bottom-effect artefact, which is experimentally demonstrated to be able to restore (at the 4^{th} correction order) a sample Young modulus as an intrinsic material property, *i.e.* a Young modulus value independent from the thickness of the film and not perturbed by the presence of a rigid substrate. These observations are validated by finite element method (FEM) simulations.

Moreover, it is shown that indenting not more than 10-20% of the sample thickness (in this case *ca.* 1 nm), *does not* ensure that the nanomechanical contribution of the rigid substrate is negligible. Indeed, the crucial parameter to determine whether the bottom-effect artefact is relevant, is the ratio between the *contact radius* (and not the pure indentation) and the sample thickness.

The amphiphilic chemical structure of the material here investigated is representative of several kinds of biological materials, therefore paving the way for future determinations of the *correct* Young modulus of supported lipid membranes. Due to the generality of Garcia's bottom-effect correction theory, we foresee applications to every kind of supported soft sample fields, from (ultra-) thin film technologies to mechanobiology, where the measured apparent elastic modulus of a cell can strongly depend on the location of the indentation. Nonetheless, we consider our approach to the

bottom-effect artefact/correction to be valid only inside the AFM community and not the whole nanomechanics field for which additional experiments are needed.

4. Experimental Section

Atomic Force Microscopy (AFM) imaging and force-spectroscopy:

AFM measurements were performed at room temperature, about 25 °C, using a Multimode 8 (Bruker) AFM microscope. SCANASYST FLUID+ (Bruker) cantilevers were used both for topography and nanomechanical measurements in a liquid environment, namely 10 mM HEPES, 300 mM NaCl, 20 mM $MgCl_2$, pH = 7.4. The cantilevers were used as received for the AFM imaging and nanomechanical experiments. To avoid damaging the tip, the calibration procedures[55] were performed at the end of the AFM force-spectroscopy (AFM-FS) experiment. The deflection sensitivity *S*, was obtained by performing ten force-distance curves on mica (in the same liquid environment and without changing the laser spot position onto the cantilever) and calculating the average inverse slope of the contact region. The cantilevers spring constant (*ca.* 0.7 $N \cdot m^{-1}$) was then obtained (in liquid as well) using the standard thermal tune method.[55]

The used cantilever has a nominal cantilever bending angle smaller than 2°, therefore no trigonometrical correction was applied to the force calculations and to the finite element method (FEM) simulations where a vertical indenting tip was used.

The breakthrough force experiments were carried out following the AFM-FS method. After recording a 2 x 2 μm^2 topographical image, on the same scanned region, an array of 20 x 20 points was selected, resulting in a distance between close pixels of 100 nm, much bigger than twice the measured tip radius (R = 17 nm) to avoid breakthrough holes overlapping. Force-distance curves were recorded by approaching

and retracting the cantilever tip to the sample (for about 150 nm) at a constant speed (1 $\mu m \cdot s^{-1}$), with 1024 pixels in the vertical direction and about 4 V as a deflection set-point. All the AFM images were obtained in tapping mode at about 1 Hz of scan rate. These were all equally post processed with Gwyddion[56] by means of a plane flattening, a 2nd order polynomial flattening in *x* and *y*, plus a median of difference rows alignment.

As described in the SI (Section 6), the tip radius *R* was measured before and after the official bottom-effect experiment, using a commercial polystyrene and polyolefin elastomer (ethylene-octene copolymer) PS-LDPE test sample (Bruker) with a known Young modulus. The average result was $R = (17 \pm 2)$ nm.

Finite element method (FEM) simulations:

The numerical simulations of the indentation were performed with commercial FEM software (COMSOL Multiphysics, COMSOL AB, Stockholm, Sweden). The indenter was a rigid sphere (R = 17 nm), and the material model used for it was an elastic material (linear, isotropic and homogeneous, E = 170 GPa). The sample was also simulated as an elastic material (linear, isotropic and homogeneous with a Young modulus E = 130 MPa. This value was taken as the average between the two mean elastic modulus values present in Figure 3d, *i.e.* 134 and 125 MPa). The lateral size of the sample (100 nm) was large enough to prevent lateral boundary effects, and two different thickness were simulated (h_1 = 7 nm and h_2 = 14 nm). The bottom of the sample was fixed to a rigid substrate. The tip was moved perpendicular to the sample surface, up to a maximum indentation of 1 nm.

The mesh parameters were refined until a convergence in the solutions was obtained. This final converged mesh was graded to be more refined close to the indenter

and in the surroundings of the tip contact point (0.01 nm) and coarser at the edges of the sample (up to 0.1 nm). The simulations were performed assuming a frictionless contact between the tip and the sample.

Supporting Information

Additional data concerning the synthesis of the glycosphingolipid, the fabrication of the glycosphingolipid supported lipid membrane, its characterization by contact angle, by zeta-potential, the Nanomechanics Python code to analyze all the force-distance curves and, finally, the AFM tip radius measurements.

Acknowledgements

S.C., S.M. and P.C. are grateful for financial assistance from the European MagicCellGene Project (M-ERA.NET COFUND call 2016, Ministerio de Economía y Competitividad from Spain in the framework of project PCIN-2017-127). P.C. and S.M. also acknowledge support from DGA and Fondos FEDER for funding Platon research group (E31_17R). K.K. and D.B.W. are grateful to the German Science Foundation (SFB 803, project A05) for financial support. Authors acknowledge Javier Idiago for providing the AFM HEPES buffer. We are also indebted to Prof. Ricardo Garcia for useful discussions and Prof. Luca Costa for the Python code that was used and expanded in this work.

Competing financial interests

Authors declare they have no competing financial interests.

References:

1. Roca-Cusachs, P.; Conte, V.; Trepat, X., *Nature Cell Biology* **2017,** *19*, 742-751.
2. Paluch, E. K.; Nelson, C. M.; Biais, N.; Fabry, B.; Moeller, J.; Pruitt, B. L.; Wollnik, C.; Kudryasheva, G.; Rehfeldt, F.; Federle, W., *BMC Biology* **2015,** *13* (1), 47-61.
3. Krieg, M.; Fläschner, G.; Alsteens, D.; Gaub, B. M.; Roos, W. H.; Wuite, G. J. L.; Gaub, H. E.; Gerber, C.; Dufrêne, Y. F.; Müller, D. J., *Nat. Rev. Phys.* **2019,** *1* (1), 41-57.
4. Mandriota, N.; Friedsam, C.; Jones-Molina, J. A.; Tatem, K. V.; Ingber, D. E.; Sahin, O., *Nat. Mater.* **2019,** *18* (10), 1071-1077.
5. Lekka, M.; Laidler, P.; Gil, D.; Lekki, J.; Stachura, Z.; Hrynkiewicz, A. Z., *European Biophysics Journal* **1999,** *28* (4), 312-316.
6. Fuhrmann, A.; Staunton, J. R.; Nandakumar, V.; Banyai, N.; Davies, P. C. W.; Ros, R., *Physical biology* **2011,** *8* (1), 015007-015007.
7. Plodinec, M.; Loparic, M.; Monnier, C. A.; Obermann, E. C.; Zanetti-Dallenbach, R.; Oertle, P.; Hyotyla, J. T.; Aebi, U.; Bentires-Alj, M.; Lim, R. Y. H.; Schoenenberger, C.-A., *Nat. Nanotechnol.* **2012,** *7* (11), 757-765.
8. Gumí-Audenis, B.; Costa, L.; Redondo-Morata, L.; Milhiet, P.-E.; Sanz, F.; Felici, R.; Giannotti, M. I.; Carlà, F., *Nanoscale* **2018,** *10* (1), 87-92.
9. Gumí-Audenis, B.; Giannotti, M. I., Structural and Mechanical Characterization of Supported Model Membranes by AFM. In *Biomimetic Lipid Membranes: Fundamentals, Applications, and Commercialization*, Kök, F. N.; Arslan Yildiz, A.; Inci, F., Eds. Springer International Publishing: Cham, 2019; pp 1-27.
10. Roiter, Y.; Ornatska, M.; Rammohan, A. R.; Balakrishnan, J.; Heine, D. R.; Minko, S., *Nano Letters* **2008,** *8* (3), 941-944.
11. Lee, K.; Zhang, L.; Yi, Y.; Wang, X.; Yu, Y., *ACS Nano* **2018,** *12* (4), 3646-3657.
12. Chiodini, S.; Reinares-Fisac, D.; Espinosa, F. M.; Gutiérrez-Puebla, E.; Monge, A.; Gándara, F.; Garcia, R., *Scientific Reports* **2017,** *7* (1), 11088-11094.
13. Zuttion, F.; Redondo-Morata, L.; Marchesi, A.; Casuso, I., High-Resolution and High-Speed Atomic Force Microscope Imaging. In *Nanoscale Imaging: Methods and Protocols*, Lyubchenko, Y. L., Ed. Springer New York: New York, NY, 2018; pp 181-200.
14. Haro, M.; Giner, B.; Lafuente, C.; López, M. C.; Royo, F. M.; Cea, P., *Langmuir* **2005,** *21* (7), 2796-2803.
15. Villares, A.; Martín, S.; Giner, I.; Díaz, J.; Lydon, D. P.; Low, P. J.; Cea, P., *Soft Matter* **2008,** *4* (7), 1508-1514.
16. Ruiz-Rincón, S.; González-Orive, A.; de la Fuente, J. M.; Cea, P., *Langmuir* **2017,** *33* (30), 7538-7547.
17. Gumí-Audenis, B.; Sanz, F.; Giannotti, M. I., *Soft Matter* **2015,** *11* (27), 5447-5454.
18. Gumí-Audenis, B.; Costa, L.; Carlá, F.; Comin, F.; Sanz, F.; Giannotti, I. M., *Membranes* **2016,** *6* (4), 58-77.
19. Redondo-Morata, L.; Giannotti, M. I.; Sanz, F., *Langmuir* **2012,** *28* (35), 12851-12860.
20. Asakawa, H.; Fukuma, T., *Nanotechnology* **2009,** *20* (26), 264008-264015.
21. Trewby, W.; Faraudo, J.; Voïtchovsky, K., *Nanoscale* **2019,** *11* (10), 4376-4384.
22. Fukuma, T.; Higgins, M. J.; Jarvis, S. P., *Physical Review Letters* **2007,** *98* (10), 106101-106101(4).
23. Fukuma, T.; Higgins, M. J.; Jarvis, S. P., *Biophysical journal* **2007,** *92* (10), 3603-3609.
24. Picas, L.; Rico, F.; Scheuring, S., *Biophysical Journal* **2012,** *102* (1), L01-L03.
25. Amo, C. A.; Perrino, A. P.; Payam, A. F.; Garcia, R., *ACS Nano* **2017,** *11* (9), 8650-8659.
26. Kocun, M.; Labuda, A.; Meinhold, W.; Revenko, I.; Proksch, R., *ACS Nano* **2017,** *11* (10), 10097-10105.
27. Al-Rekabi, Z.; Contera, S., *Proc. Natl. Acad. Sci. U.S.A.* **2018,** *115* (11), 2658-2663.
28. Rother, J.; Nöding, H.; Mey, I.; Janshoff, A., *Open Biol.* **2014,** *4* (5), 140046-140046.
29. Ma, Z.; Wen, H.; Guo, H.; Tang, J.; Liu, J.; Li, Y.; Sugawara, Y., *Coatings* **2020,** *10* (84).
30. Park, W.; Müller, S.; Baumann, R.-P.; Becker, S.; Hwang, B., *Applied Surface Science* **2020,** *507*, 145041.

31. Lee, M.; Reddi, R. K. R.; Choi, J.; Liu, J.; Huang, X.; Cho, H.; Kim, J.-H., *ACS Applied Energy Materials* **2020,** *3* (2), 1899-1907.
32. F. Dufrêne, Y.; Boland, T.; W. Schneider, J.; R. Barger, W.; U. Lee, G., *Faraday Discussions* **1999,** *111* (0), 79-94.
33. Garcia-Manyes, S.; Sanz, F., *Biochimica et Biophysica Acta (BBA) - Biomembranes* **2010,** *1798* (4), 741-749.
34. Li, J. K.; Sullan, R. M. A.; Zou, S., *Langmuir* **2011,** *27* (4), 1308-1313.
35. Sneddon, I. N., *Int. J. Eng. Sci.* **1965,** *3* (1), 47-57.
36. Harding, J. W.; Sneddon, I. N., *Math. Proc. Cambridge Philos. Soc.* **2008,** *41* (1), 16-26.
37. Hertz, H., Ueber die Berührung fester elastischer Körper. In *Journal für die reine und angewandte Mathematik (Crelle's Journal)*, **1882**; Vol. 1882, p 156.
38. Popov, L. V.; Heb, M.; Willert, E., *Handbook of contact mechanics. Exact solutions of axisymmetric contact problems*. Springer: **2019**.
39. Dimitriadis, E. K.; Horkay, F.; Maresca, J.; Kachar, B.; Chadwick, R. S., *Biophys. J.* **2002,** *82* (5), 2798-2810.
40. Gavara, N.; Chadwick, R. S., *Nature Nanotechnology* **2012,** *7*, 733.
41. Garcia, P. D.; Garcia, R., *Biophysical Journal* **2018,** *114* (12), 2923-2932.
42. Garcia, P. D.; Garcia, R., *Nanoscale* **2018,** *10* (42), 19799-19809.
43. Doss, B. L.; Rahmani Eliato, K.; Lin, K.-h.; Ros, R., *Soft Matter* **2019,** *15* (8), 1776-1784.
44. Perrino, A. P.; Garcia, R., *Nanoscale* **2016,** *8* (17), 9151-9158.
45. Li, L.; Zhang, P.; Li, J.; Wang, Y.; Wei, Y.; Hu, J.; Zhou, X.; Xu, B.; Li, B., *Nanoscale* **2019,** *11* (11), 4707-4711.
46. Tero, R., *Materials* **2012,** *5* (12), 2658-2680.
47. Richter, R. P.; Brisson, A. R., *Biophysical journal* **2005,** *88* (5), 3422-3433.
48. Johnson, S. J.; Bayerl, T. M.; McDermott, D. C.; Adam, G. W.; Rennie, A. R.; Thomas, R. K.; Sackmann, E., *Biophysical journal* **1991,** *59* (2), 289-294.
49. Müller, D. J.; Engel, A., *Biophysical journal* **1997,** *73* (3), 1633-1644.
50. Redondo-Morata, L.; Giannotti, M. I.; Sanz, F., *Molecular Membrane Biology* **2014,** *31* (1), 17-28.
51. Gavara, N., *Scientific Reports* **2016,** *6*, 21267-21280.
52. Voïtchovsky, K.; Antoranz Contera, S.; Kamihira, M.; Watts, A.; Ryan, J. F., *Biophysical Journal* **2006,** *90* (6), 2075-2085.
53. Timoshenko, S., *Strength of materials. part 1. Elementary theory and problems*. New York: Van Nostrand Reinhold **1980**.

54. Espinosa, G.; López-Montero, I.; Monroy, F.; Langevin, D., *Proceedings of the National Academy of Sciences* **2011,** *108* (15), 6008.
55. Schillers, H.; Rianna, C.; Schäpe, J.; Luque, T.; Doschke, H.; Wälte, M.; Uriarte, J. J.; Campillo, N.; Michanetzis, G. P. A.; Bobrowska, J.; Dumitru, A.; Herruzo, E. T.; Bovio, S.; Parot, P.; Galluzzi, M.; Podestà, A.; Puricelli, L.; Scheuring, S.; Missirlis, Y.; Garcia, R.; Odorico, M.; Teulon, J.-M.; Lafont, F.; Lekka, M.; Rico, F.; Rigato, A.; Pellequer, J.-L.; Oberleithner, H.; Navajas, D.; Radmacher, M., *Scientific reports* **2017,** *7* (1), 5117-5117.
56. Gwyddion www.gwyddion.net.

For Table of Contents Only:

An AFM force-spectroscopy experiment is designed to investigate the so-called bottom-effect artefact affecting the nanomechanical properties of a supported lipid bilayer. While standard contact mechanics does not compensate this artefact, a full support is provided to Garcia's theory as the proper approach to measure the correct Young modulus of soft samples supported on rigid substrates.

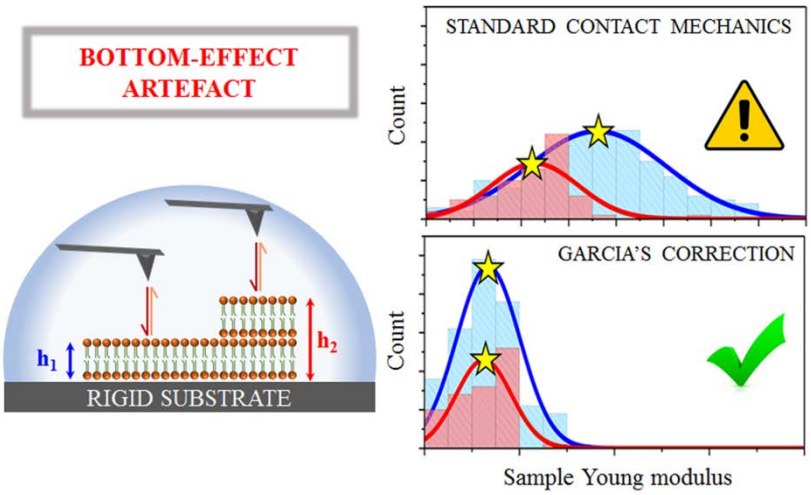

Supporting Information for

Bottom-effect in atomic force microscopy nanomechanics

Dr. Stefano Chiodini, Silvia Ruiz-Rincón†, Dr. Pablo D. Garcia†, Dr. Santiago Martin, Dr. Katharina Kettelhoit, Dr. Ilaria Armenia, Prof. Daniel B. Werz, Prof. Pilar Cea**

Table of Contents

1. Synthetic protocol for the glycosphingolipid

The structure of the synthetic glycosphingolipid (GSL) used in this contribution is shown in Figure 1a of the manuscript. The monosaccharide part of the molecule is a β-D glucose which is a D-glucopyranose with β-configuration at the anomeric centre.

- Compound **1**) O-(2,3,4,6-Tetra-O-benzoyl-β-D-glucopyranosyl)-(1→1)-(2S,3R,4E)-2-azido-3-O-pivaloyl-4-octadecene-1,3-diol (**1**)

2,3,4,6-Tetra-O-benzoyl-D-glucopyranosyl trichloroacetimidate (according to[1]) (300 mg, 0.405 mmol, 1.00 eq.) and azidosphingosine (331 mg, 0.810 mmol, 2.00 eq.) were azeotroped with toluene (3×), dried in high vacuum for 1 h and dissolved in dry dichloromethane (8.0 mL). Molecular sieves (3 Å) were added and the mixture was stirred at ambient temperature for 20 min. $BF_3{\cdot}OEt_2$ (10.0 µL, 11.5 mg, 81.0 µmol, 20.0 mol%) was added at 0 °C and the reaction mixture was allowed to slowly warm to ambient temperature. After 28 h, the reaction was stopped by adding pyridine (0.1 mL), the molecular sieves were filtered off and the solvent was removed under reduced pressure. Column chromatography on silica gel (n pentane/ethyl acetate, 10:1) afforded glucoside 1 (325 mg, 0.329 mmol, 81 %) as a colourless oil.

$[\alpha]_D^{24}$= +6.98 (c 2.24, $CHCl_3$).

^{1}H-NMR (600 MHz, $CDCl_3$): δ (ppm) = 0.88 (t, J = 7.1 Hz, 3 H), 1.15 (s, 9 H), 1.17–1.32 (m, 22 H), 1.86–1.94 (m, 2 H), 3.58 (dd, J = 10.2, 5.5 Hz, 1 H), 3.74–3.81 (m, 1 H), 3.88 (dd, J = 10.2, 6.9 Hz, 1 H), 4.17 (ddd, J = 9.7, 5.1, 3.2 Hz, 1 H), 4.51 (dd, J = 12.2, 5.1 Hz, 1 H), 4.64 (dd, J = 12.1, 3.2 Hz, 1 H), 4.87 (d, J = 7.8 Hz, 1 H), 5.26 (dd, J = 8.0, 4.2 Hz, 1 H), 5.29–5.36 (m, 1 H), 5.55 (dd, J = 9.7, 7.8 Hz, 1 H), 5.58–5.66

(m, 1 H), 5.69 (t, J = 9.7 Hz, 1 H), 5.91 (t, J = 9.7 Hz, 1 H), 7.26–7.45 (m, 9 H), 7.46–7.58 (m, 3 H), 7.78–8.06 (m, 8 H).

^{13}C-NMR (151 MHz, $CDCl_3$): δ (ppm) = 14.1, 22.7, 27.0, 28.6, 29.0, 29.3, 29.4, 29.6, 29.6, 29.7, 29.7, 29.7, 31.9, 32.2, 38.8, 63.0, 63.4, 68.1, 69.5, 71.6, 72.4, 72.8, 73.9, 100.9, 122.7, 128.3, 128.3, 128.4, 128.4, 128.7, 128.7, 129.2, 129.5, 129.7, 129.8, 129.8, 129.8, 133.2, 133.2, 133.3, 133.4, 138.4, 164.9, 165.1, 165.8, 166.1, 176.3.

IR (ATR): $\tilde{\nu}$ (cm^{-1}) = 2925, 2854, 2102, 1725, 1601, 1452, 1261, 1091, 1066, 1027, 756, 707.

MS (ESI): m/z (%) = 1999.0 (38) $[2M+Na]^+$, 1010.5 (100) $[M+Na]^+$. HRMS (ESI): m/z calculated for $C_{57}H_{69}N_3O_{12}$: $[M+Na]^+$: 1010.4774, found: 1010.4778.

- Compound **2**) O-(2,3,4,6-Tetra-O-benzoyl-β-D-glucopyranosyl)-(1→1)-(2S,3R,4E)-2 (tetracosanamido)-3-O-pivaloyl-4-octadecene-1,3-diol (**2**)

To a solution of azide 1 (184 mg, 0.186 mmol, 1.00 eq.) in benzene (9.5 mL) were added triphenylphosphine (112 mg, 0.428 mmol, 2.30 eq.) and water (0.70 mL). The suspension was heated to 60 °C (oil bath temperature) for 16 h. The solvents were removed under reduced pressure; subsequently the residue was azeotroped with toluene (3×) and dried in high vacuum for 1 h. The residue was dissolved in dry THF (7.5 mL) to which tetracosanoic acid (89.0 mg, 0.242 mmol, 1.30 eq.) and DIPEA (41.0 µL, 31.0 mg, 0.242 mmol, 1.30 eq.) were added. Afterwards, a solution of HATU (92.0 mg, 0.242 mmol, 1.30 eq.) in dry DMF (3.7 mL) was added dropwise at ambient temperature. After 3 h the reaction was stopped by adding ethyl acetate and sat. aq. NaCl solution. The organic layer was washed with sat. aq. NaCl solution (2×) and the combined aqueous phases were reextracted with ethyl acetate. The combined organic layers were dried over Na_2SO_4, filtered and concentrated under reduced pressure. Gel

permeation HPLC afforded glycolipid 2 (142 mg, 0.108 mmol, 58 %) as a colourless solid.

$[\alpha]_D^{27}$ = +7.94 (c 1.39, $CHCl_3$).

^{1}H-NMR (600 MHz, $CDCl_3$): δ (ppm) = 0.83–0.93 (m, 6 H), 1.13 (s, 9 H), 1.18–1.31 (m, 62 H), 1.57–1.68 (m, 2 H), 1.70 (t, J = 7.7 Hz, 2 H), 1.96 (dd, J = 13.9, 6.9 Hz, 2 H), 3.58 (dd, J = 9.8, 3.8 Hz, 1 H), 4.10 (dd, J = 9.8, 2.9 Hz, 1 H), 4.15 (ddd, J = 9.8, 5.0, 3.2 Hz, 1 H), 4.28–4.34 (m, 1 H), 4.46 (dd, J = 12.2, 5.0 Hz, 1 H), 4.61 (dd, J = 12.2, 3.2 Hz, 1 H), 4.79 (d, J = 7.8 Hz, 1 H), 5.22 (t, J = 7.4 Hz, 1 H), 5.32 (dd, J = 15.3, 7.4 Hz, 1 H), 5.49 (dd, J = 9.8, 7.8 Hz, 1 H), 5.55 (d, J = 9.3 Hz, 1 H), 5.68 (t, J = 9.8 Hz, 1 H), 5.70–5.76 (m, 1 H), 5.88–5.96 (m, 1 H), 7.21–7.37 (m, 5 H), 7.37–7.46 (m, 5 H), 7.46–7.59 (m, 3 H), 7.79–8.04 (m, 7 H).

^{13}C-NMR (151 MHz, $CDCl_3$): δ (ppm) = 13.9, 22.5, 25.3, 26.8, 28.8, 29.0, 29.2, 29.2, 29.3, 29.4, 29.4, 29.5, 29.5, 29.5, 29.5, 31.7, 32.0, 33.4, 36.2, 38.5, 50.0, 62.8, 67.7, 69.2, 72.0, 72.1, 72.4, 72.8, 101.0, 124.8, 128.1, 128.2, 128.2, 128.3, 128.5, 128.5, 128.8, 129.2, 129.5, 129.5, 129.6, 129.6, 133.0, 133.1, 133.3, 133.3, 136.7, 164.9, 164.9, 165.5, 165.9, 172.3, 176.7.

IR (ATR): $\tilde{\nu}$ (cm^{-1}) = 2918, 2850, 2160, 1727, 1652, 1538, 1453, 1262, 1159, 1095, 1067, 1027, 706.

MS (ESI): m/z (%) = 1334.8 (100) $[M+Na]^+$. HRMS (ESI): m/z calculated for $C_{81}H_{117}NO_{13}$: $[M+Na]^+$: 1334.8417, found: 1334.8418.

- Compound **3**) O-(β-D-Glucopyranosyl)-(1→1)-(2S,3R,4E)-2-(tetracosanamido)-4-octadecene-1,3-diol (**3**)

Protected glycolipid **2** (127 mg, 96.7 µmol, 1.00 eq) was dissolved in a mixture of methanol (4.8 mL) and dichloromethane (1.6 mL). Sodium methoxide (5.4 M in MeOH) was added at ambient temperature until a pH value >12 was reached. The reaction mixture was stirred at 50 °C for 21 h, neutralized with Amberlite®, filtered and concentrated in vacuo. After a dialysis of **2** d with 5 L of H2O and subsequent lyophilization glycolipid **3**, the target compound (74.0 mg, 91.0 µmol, 94 %), was obtained as a colourless powder.

$[\alpha]_D^{23} = -9.40$ (c 1.08, $CHCl_3$/MeOH/H_2O, 1.6:1.0:0.2).

^{1}H-NMR (600 MHz, $CDCl_3$/MeOD/D_2O, 1.6:1.0:0.2): δ (ppm) = 0.70–1.01 (m, 6 H), 1.13–1.48 (m, 62 H), 1.52–1.64 (m, 2 H), 1.99–2.06 (m, 2 H), 2.17 (t, J = 7.7 Hz, 2 H), 3.27 (dd, J = 9.1, 7.9 Hz, 1 H), 3.30 (ddd, J = 9.6, 5.3, 2.3 Hz, 1 H), 3.37 (t, J = 9.1 Hz, 1 H). 3.42 (t, J = 9.1 Hz, 1 H), 3.59 (dd, J = 10.1, 3.1 Hz, 1 H), 3.71 (dd, J = 12.2, 5.3 Hz, 1 H), 3.86 (dd, J = 12.2, 2.2 Hz, 1 H), 3.95–4.00 (m, 1 H), 4.07 (t, J = 7.9 Hz, 1 H), 4.17 (dd, J = 10.1, 4.4 Hz, 1 H), 4.30 (d, J = 7.9 Hz, 1 H), 5.44 (dd, J = 15.3, 7.9 Hz, 1 H), 5.66–5.74 (m, 1 H).

^{13}C-NMR (151 MHz, $CDCl_3$/MeOD/D_2O, 1.6:1.0:0.2): δ (ppm) = 14.5, 14.5, 23.2, 23.2, 26.6, 29.9, 29.9, 29.9, 30.0, 30.0, 30.1, 30.2, 30.2, 30.2, 30.3, 30.3, 30.3, 30.3, 32.5, 32.5, 33.0, 37.1, 53.8, 66.7, 69.4, 70.4, 72.3, 74.1, 76.8, 76.8, 103.6, 129.8, 135.3, 157.4.

IR (ATR): $\tilde{\nu}$ (cm^{-1}) = 3295, 2955, 2916, 2849, 1709, 1643, 1544, 1467, 1291, 1077, 1035, 720.

MS (ESI): m/z (%) = 834.7 (100) $[M+Na]^+$. HRMS (ESI): m/z calculated for $C_{48}H_{93}NO_8$: $[M+Na]^+$: 834.6793, found: 834.6796.

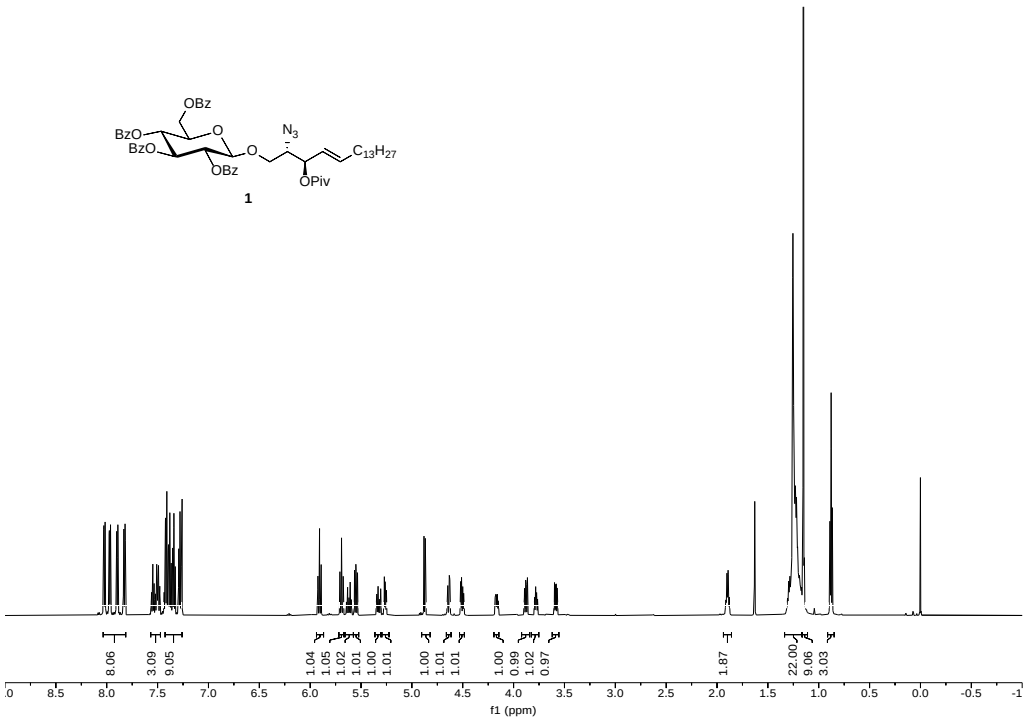

Figure S1. ^{1}H-NMR spectrum of compound **1** ($CDCl_3$, 600 MHz)

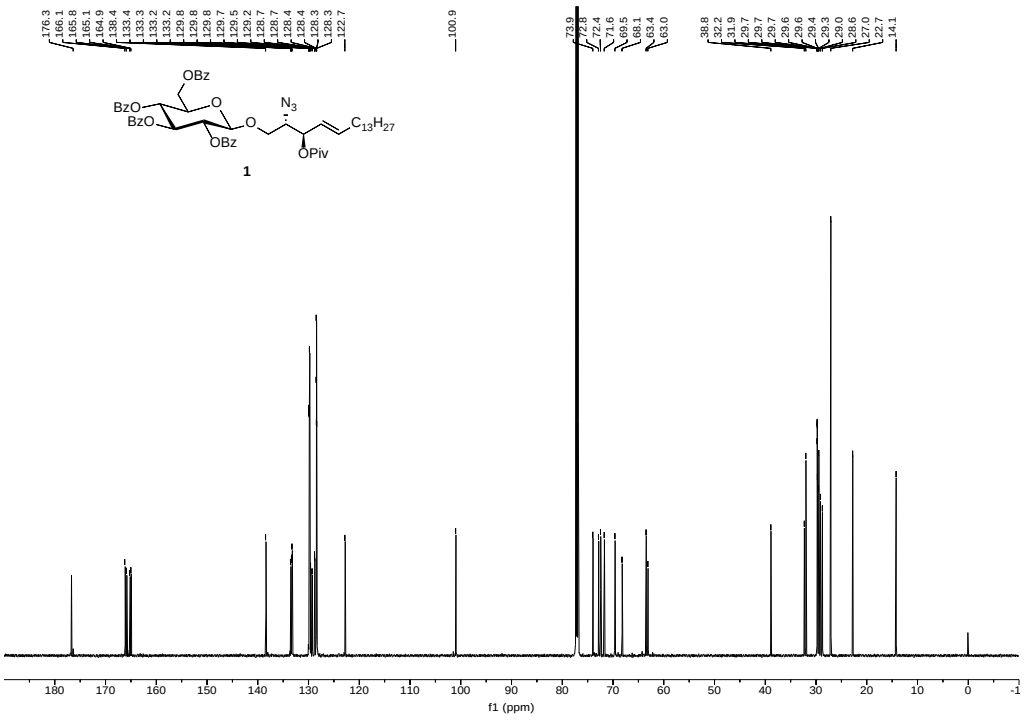

Figure S2. ^{13}C-NMR spectrum of compound **1** ($CDCl_3$, 151 MHz)

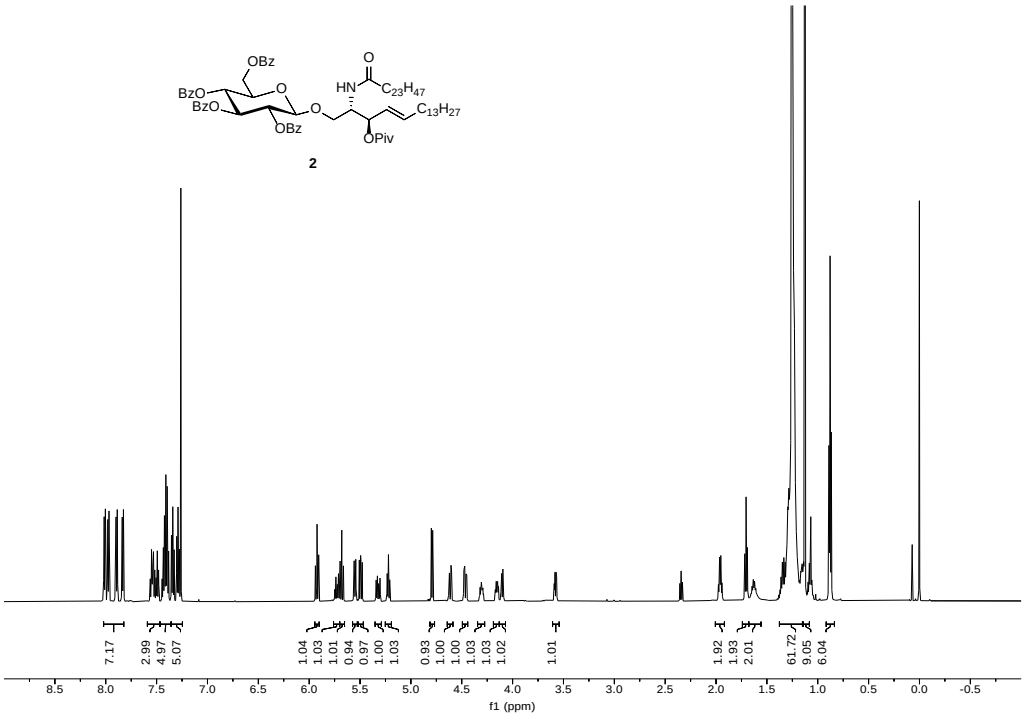

Figure S3. ^{1}H-NMR spectrum of compound **2** ($CDCl_3$, 600 MHz)

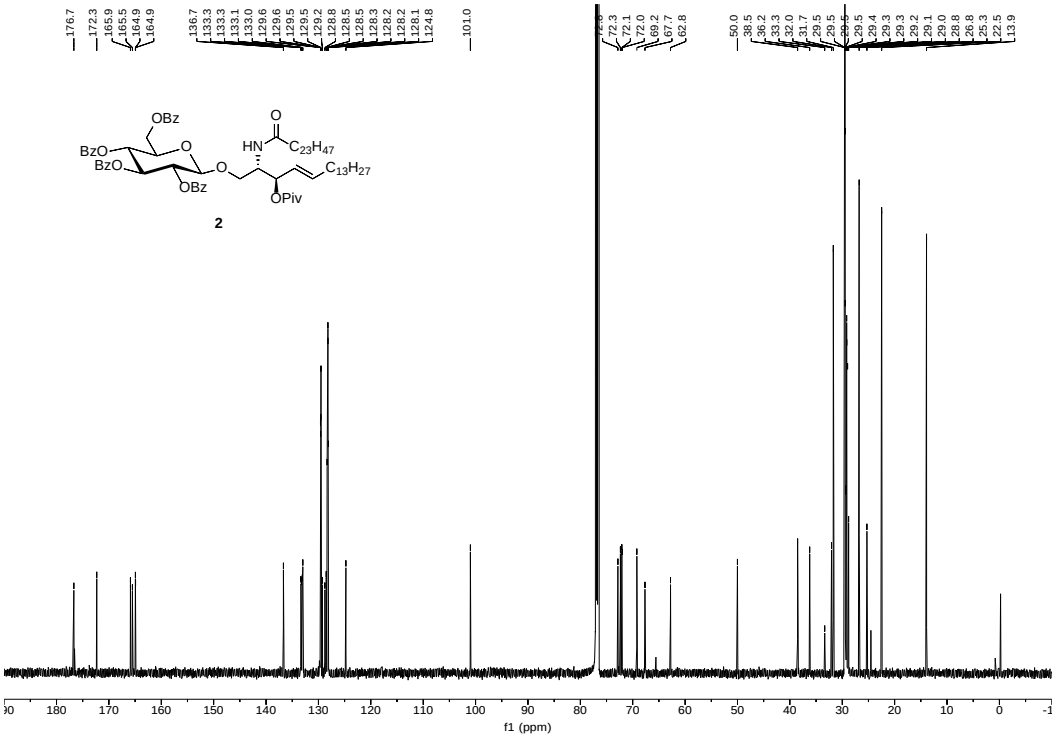

Figure S4. ^{13}C-NMR spectrum of compound **2** ($CDCl_3$, 151 MHz)

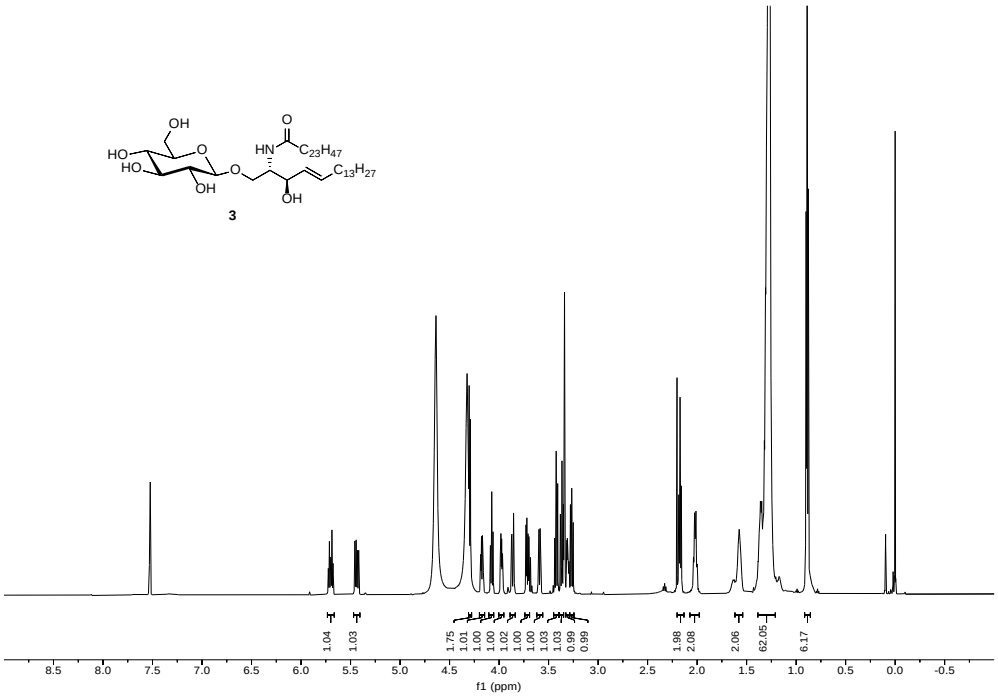

Figure S5. ^{1}H-NMR spectrum of compound **3** ($CDCl_3$/MeOD/D_2O, 600 MHz)

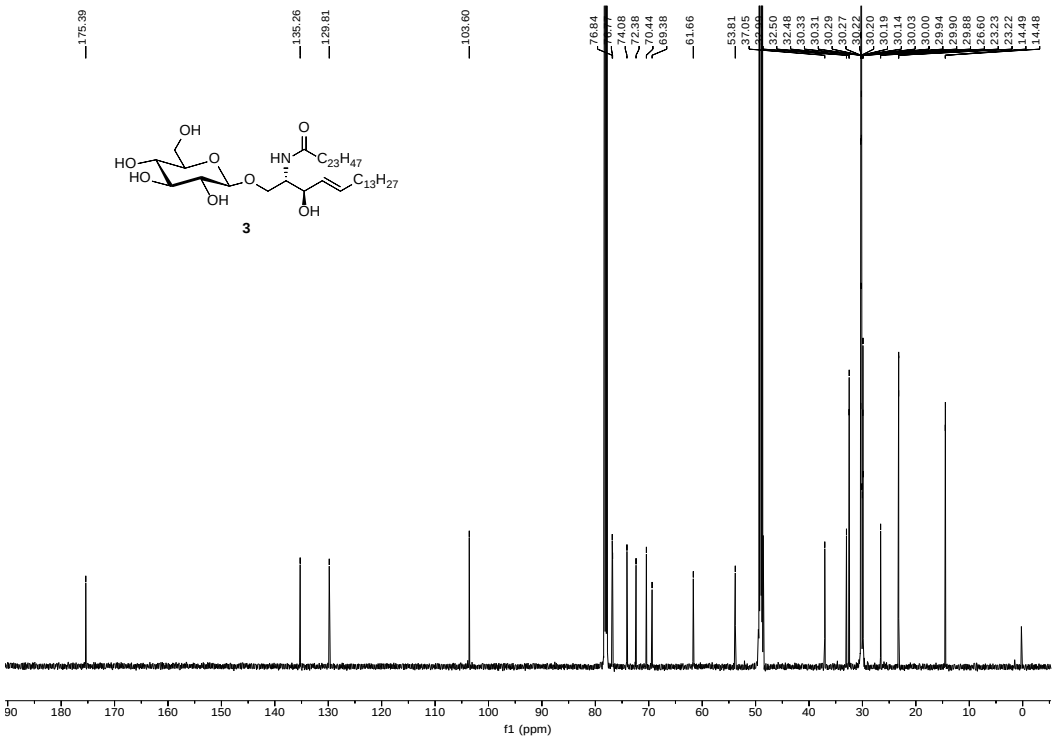

Figure S6. ^{13}C-NMR spectrum of compound **3** ($CDCl_3$/MeOD/D_2O, 151 MHz)

2. Preparation of Langmuir-Schaefer films

Langmuir-Schaefer (LS) films were prepared using a commercial trough (NIMA-KSV), which is housed in clean room at a constant temperature of (20 ± 1) ºC. 750 µL of a 10^{-4} M solution of GSL in chloroform were spread by using a Hamilton syringe, which was held very close to the surface, allowing the surface pressure to return to a value close to zero between each addition. Subsequently, the solvent was allowed to evaporate for fifteen minutes; afterwards, the film was slowly compressed at a sweeping speed of 6 $nm^2 \cdot molecule^{-1} \cdot min^{-1}$. The Langmuir films were transferred at a constant surface pressure of 8 $mN \cdot m^{-1}$ by the horizontal dipping method (the dipping speed was 1 $mm \cdot min^{-1}$) onto a freshly cleaved mica substrate to obtain Langmuir-Schaefer films incorporating the GSL.

3. Contact angle measurements

Contact angle experiments were performed with a commercial optical tensiometer (Theta Lite TL 101 from Attention). In order to measure the contact angle, the GSL supported lipid membrane (SLM) on mica was placed on a plane platform, just below a needle from which a drop of pure water was deposited onto the film surface. Thereafter, the computer software collected readings of the contact angle at different times. The process was repeated several times in distinct places of three different LS films to test the reproducibility of the data. As shown in Figure S7 the measurement of the contact angle provided a value smaller than 10°, therefore addressing a high hydrophilicity of the film surface.

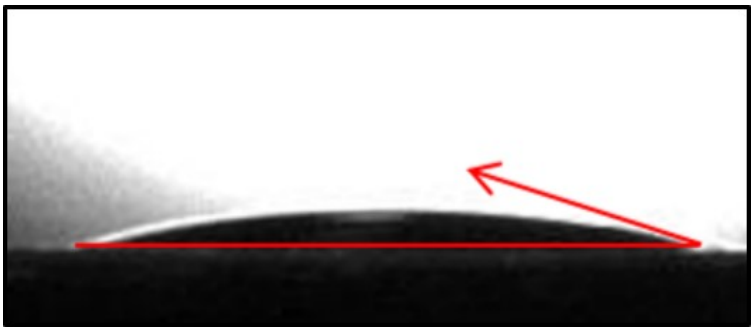

Figure S7. Representative optical image of the contact angle on top of the GSL SLM. The measurement of the contact angle provided a value smaller than 10°.

4. Zeta potential measurements

The measurements of the electrophoretic mobility (zeta potential) of the glycosphingolipid film were performed with a Zeta Plus 90 Particle Sizer (Brookhaven Instruments Corp., USA) equipped with a 5 mW He-Ne laser (633 nm). The measured zeta potential value for the GSL, (-15 ± 2) mV, is the average of ten values obtained using the Smoluchowski's equation. This zeta potential value is later used for the determination of the electric double layer (EDL) force between AFM tip and sample (Section 5c).

5. Nanomechanics Python code

5a) Baseline procedure

All the raw deflection – *Z* (piezo) data were affected by an offset in the deflection value (about -2V, see Figure S8). In order to remove it and restore a zero-deflection correspondent to the non-interaction regime (cantilever far from the sample) the common baseline procedure was achieved subtracting to the raw data the straight line connecting the two force-points relative to *Z* (piezo) = 120 nm and *Z* (piezo) = 90 nm (Figure S8).

Remarkably, from Figure S8 no adhesion can be appreciated between tip and sample. As discussed in the main text, this is a requirement in order to use Sneddon's contact mechanics model. This result is further confirmed by Figure S16 where ten force-*Z*(piezo) curves are reported. All these curves are free from any adhesion phenomenon, *i.e.* negative force.

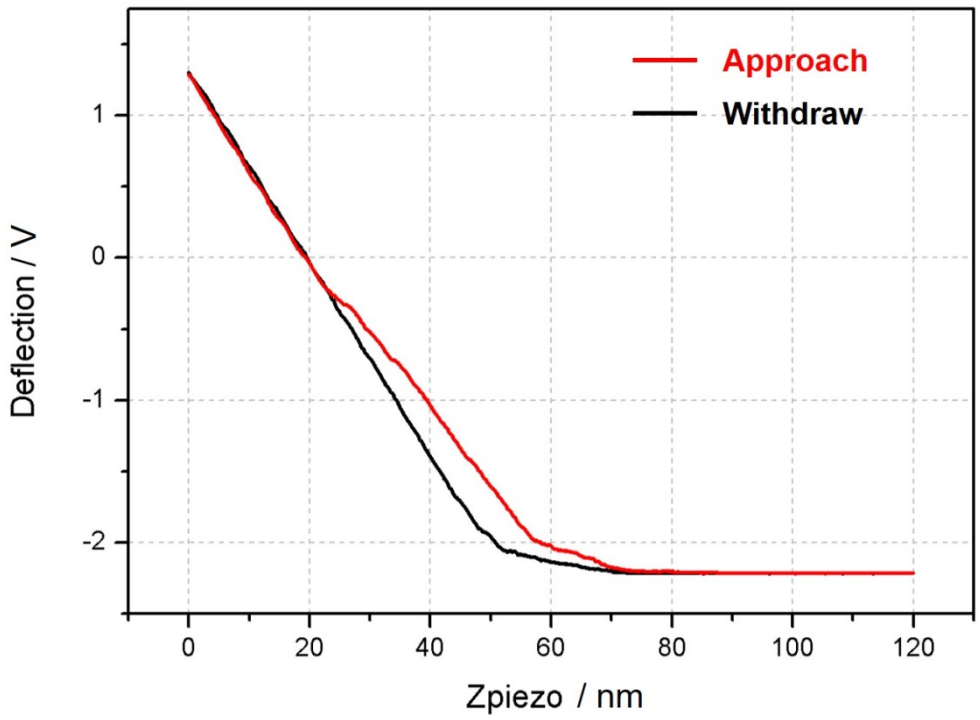

Figure S8. Representative approach (red data) and withdraw (black data) deflection – Z (piezo) raw data curves. A clear offset of the non-interaction region is visible at *ca.* - 2V.

5b) Breakthrough force histogram

All the force values were obtained using the expression: $F = k \cdot d$, with k equal to the calibrated spring constant and d corresponding to the calibrated deflection (in nm) of the cantilever. The used cantilever (SCANASYST FLUID+, Bruker), has a nominal cantilever bending angle smaller than 2°, therefore no trigonometrical correction was applied to the aforementioned force expression.

The evaluation of the breakthrough force was computationally done calculating the first derivative of the force – *Z* (piezo) curve, checking where it becomes lower than a negative threshold. This point will correspond to point B of Figure 2b.

Figure S9 shows the breakthrough force histogram obtained out of all the performed force-distance curves, showing an average breakthrough force of about 20 nN for a GSL SLM immersed in 10 mM HEPES, 300 mM NaCl and 20 mM $MgCl_2$ (pH = 7.4), at a cantilever approach speed of 1 $\mu m \cdot s^{-1}$. The order of magnitude agrees with AFM breakthrough experiments performed on similar molecules.[2]

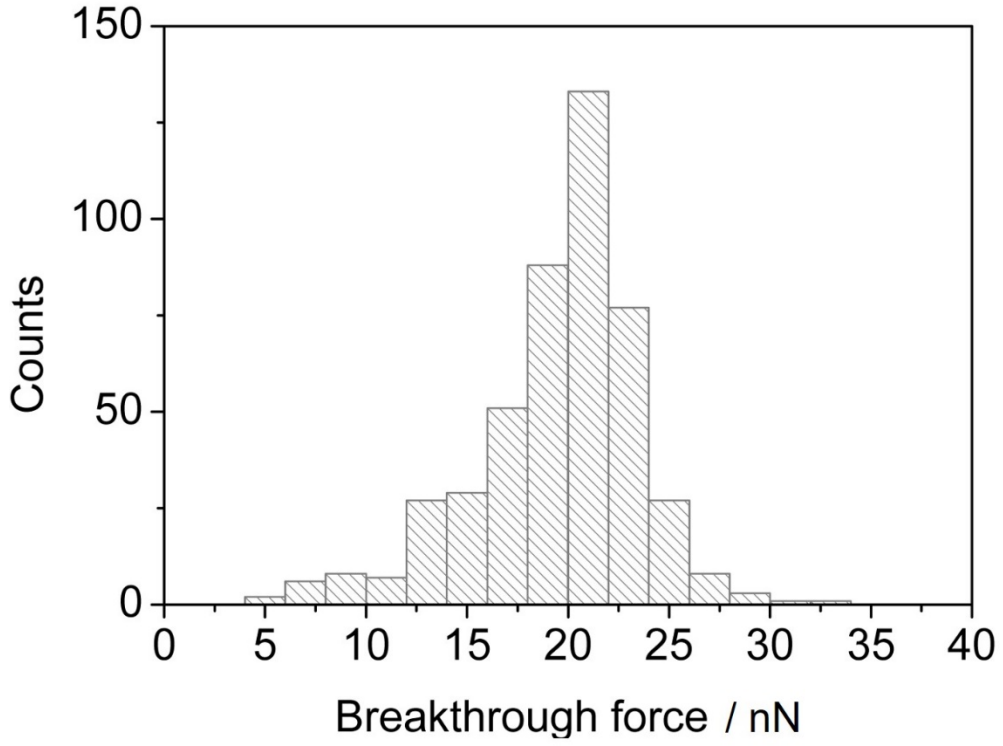

Figure S9. Breakthrough force histogram for a GSL SLM immersed in 10 mM HEPES, 300 mM NaCl and 20 mM $MgCl_2$ (pH=7.4), at a cantilever approach speed of 1 $\mu m \cdot s^{-1}$. The average value is around 20 nN.

5c) Determination of the contact point

The determination of the contact point is crucial in AFM nanomechanics, mainly for soft samples.[3] As it is clearly visible from Figure S8, and as already reported in the literature,[4] following the non-interaction regime (cantilever far from the sample), two distinct regimes can be recognized: a first increase of the force from *Z* (piezo) = 70 nm till *Z* (piezo) = 55 nm, and then a second increasing part which we consider the real indentation of the sample. The first part can be ascribed to a contribution from Derjaguin-Landau-Verwey-Overbeek (DLVO) and/or hydration forces, which should not be considered for the contact mechanics calculation (the layer of GSL molecules showed a zeta potential of about -15 mV, see Section 4). Therefore, the contact point was set at the end of the first electrostatic regime.

In order to be quantitative, the derivative of the *average* force – indentation curve was determined to detect a change of trend at the end of the first electrostatic regime (DLVO/hydration part).

In Figure S10a, the average force gradient – indentation curve is shown. In this Figure, a clear change of slope is visible at *ca.* 8 nm of indentation into the first DLVO/hydration regime. This threshold corresponds to a force of *ca.* 0.9 nN, see Figure S10b.

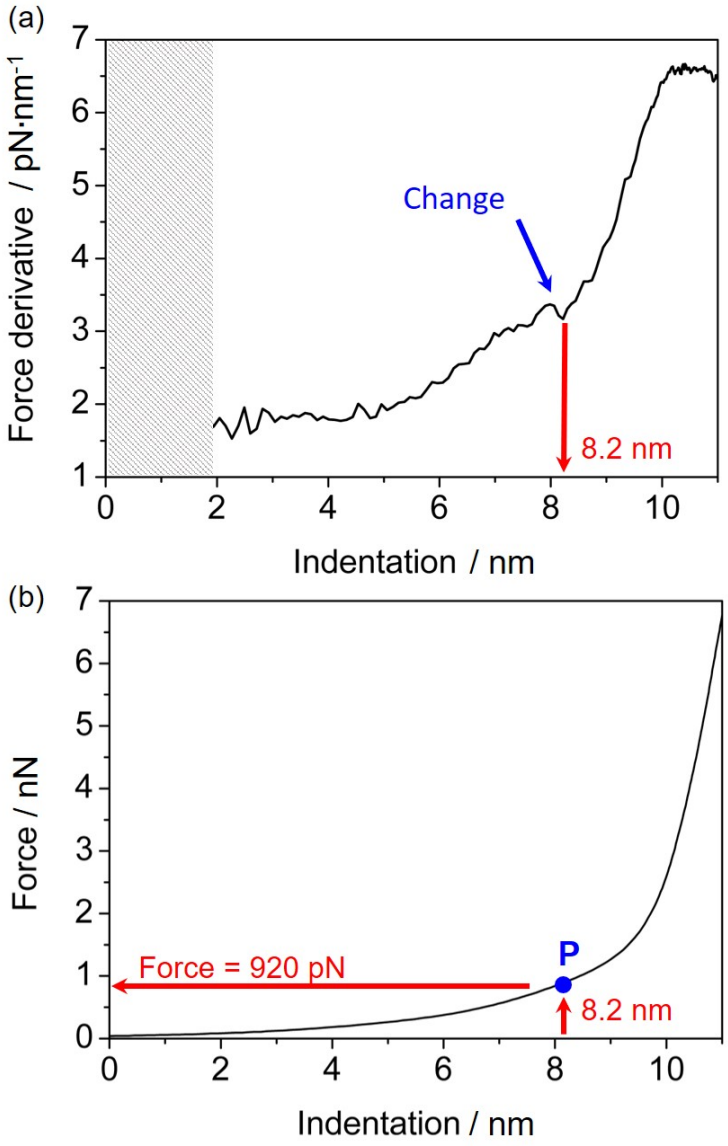

Figure S10. a) Average force gradient – indentation curve obtained from all the recorded force - distance curves. A clear change of slope is visible at an indentation value of 8.2 nm. For x < 2 nm the plot is not shown due to a border effect of the gradient calculation. b) Average force – indentation curve calculated from all the raw data. As can be appreciated, at x = 8.2 nm corresponds a force of around 0.9 nN (point P).

The *real* contact point was then selected as the point *P* = (indentation = 8.2 nm, force = 920 pN). All the nanomechanical results presented in this contribution (as illustrated in Figure 3), were obtained resetting *P* to (0, 0), therefore ruling out completely any contribution from the first electrostatic regime.

To double check the robustness of the bottom-effect artefact with respect to the contact point choice, a change of contact-point force from 800 pN to 1040 pN was allowed in the Nanomechanical Python code, correspondent to about three Angstrom of indentation shift.

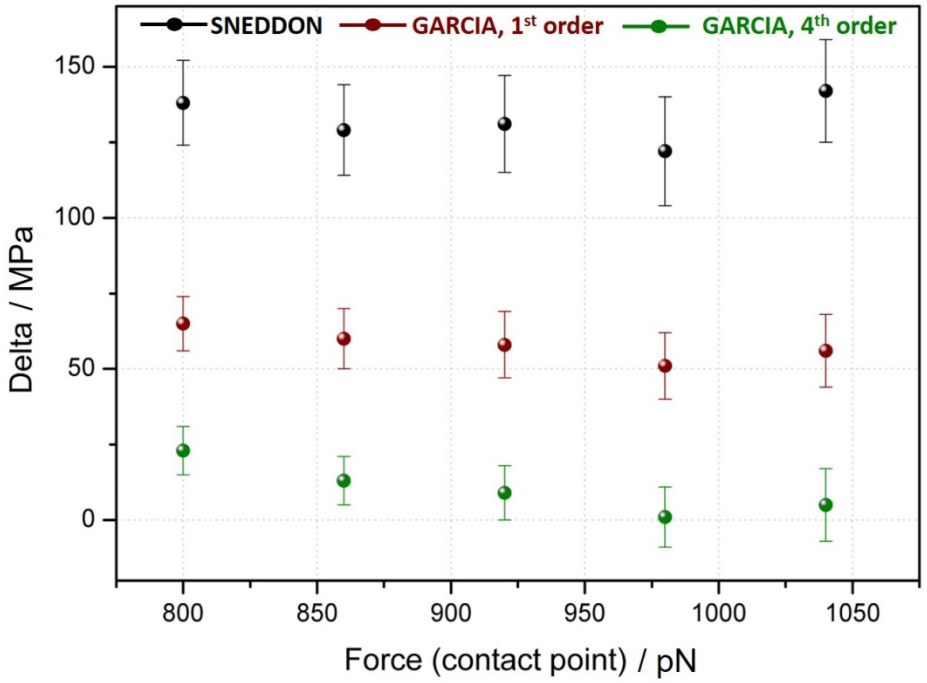

Figure S11. Delta values vs Force (contact point) plot. Delta is defined as the difference between the average Young modulus for 7 nm patches and the average Young modulus for 14 nm thick regions (see Figure 3). Main parameters used in the simulation: R = 17 nm, k = 0.6878 $N \cdot m^{-1}$, deflection sensitivity S = 14.46 $nm \cdot V^{-1}$ (for the calibration of the last two values see the AFM methods Section), χ^2 = 10, tip geometry: paraboloidal.

As shown in Figure S11, the trend of the bottom-effect artefact correction is completely preserved despite the aforementioned contact point change. Indeed, if on the one hand Sneddon's theory always provide a quite different value of *delta* (average Young modulus for 7 nm patches minus average Young modulus for 14 nm patches), on

the other hand Garcia's correction at the 4th order yields a value sensibly close to zero, with the correction at the 1st order showing a middle behaviour.

Finally, we have also tried to rationalize the first electrostatic regime, previously ascribed to DLVO/hydration forces. The DLVO force is made up of two contributions, the van der Waals and the electric double layer (EDL) force between AFM tip and sample.[5] Due to the AFM liquid environment we can assume a negligible Hamaker constant (H≃0.1 x 10^{-20} J) and rule out the contribution from the van der Waals force. The EDL force (F_{EDL}), can be evaluated as follows[5]:

$$F_{EDL} = \frac{4\pi\sigma_{sample}\sigma_{tip}R\lambda_{Debye}}{\varepsilon_0\varepsilon} e^{-z/\lambda_{Debye}}$$

with R = 17 nm (see Section 5g), z equal to the tip-sample distance, ε_0 equal to the vacuum dielectric constant and ε correspondent to the relative permittivity of water (ε = 80). The Debye length, λ_{Debye}, was calculated following its standard expression,[5] obtaining, for the used AFM liquid environment ionic strength, $\lambda_{Debye} \simeq 0.5$ nm. Since the GSL zeta potential is Φ_{GSL} = - 15 mV (Section 4), the sample surface charge density, σ_{sample}, was determined as: $\sigma_{sample} = \varepsilon_0 \cdot \varepsilon \cdot (1/\lambda_{Debye}) \cdot \Phi_{GSL} \simeq$ - 21 mC·m^{-2}. The AFM tip surface charge density was assumed to be[6],[7] $\sigma_{tip} \simeq$ - 40 mC·m^{-2}. In conclusion, a maximum value for F_{EDL} of about 100 pN is obtained, a value definitely smaller than the previously measured force at the contact point (920pN), therefore ruling out the DLVO force as the main reason for the first electrostatic regime. Hence, the hydration force which reads as follows[5]:

$$F_{hydr} = F_0 e^{-z/\lambda_{hydr}}$$

needs to be considered. Assuming this force as leading in the first electrostatic regime, its magnitude (F_0) and its extension (λ_{hydr}) were estimated from Figure S10b, obtaining: $F_0 \simeq 1$ nN and $\lambda_{hydr} \simeq 1.5$ nm.

Remarkably, these two values infer a strong hydration shell around the polar heads of the GSL molecules. As reported by Prinetti and co-workers,[8] water is an important component of sugar shells due to the high hydrophilicity of the monosaccharide (see Section 3).

5d) Determination of the height of the GSL SLM regions

The determination of the height of the GSL SLM patches was done automatically, for each force-distance curve, considering the distance - in *indentation* - between the contact point (Point A of Figure 2b) and the onset of the mica contact regime (Point D of Figure 2b).

Figure S12 shows the sample thickness histogram which exhibits three main heights, *ca.* 7 nm, 11 nm and 14 nm which we ascribe to 2-layer, 3-layer and 4-layer regions, respectively. For the nanomechanical analysis, only the force-distance curves related with the first peak (*ca.* 7 nm, N = 180 events) and the last one (*ca.* 14 nm, N = 60 events) were considered (with a thresholding procedure).

Remarkably, the calculation of the sample thickness from the force-indentation curves is strongly influenced by the choice of the contact point. The fact that Figures S12 and Figure 1c show the same thicknesses strongly supports the previously discussed choice of the contact point.

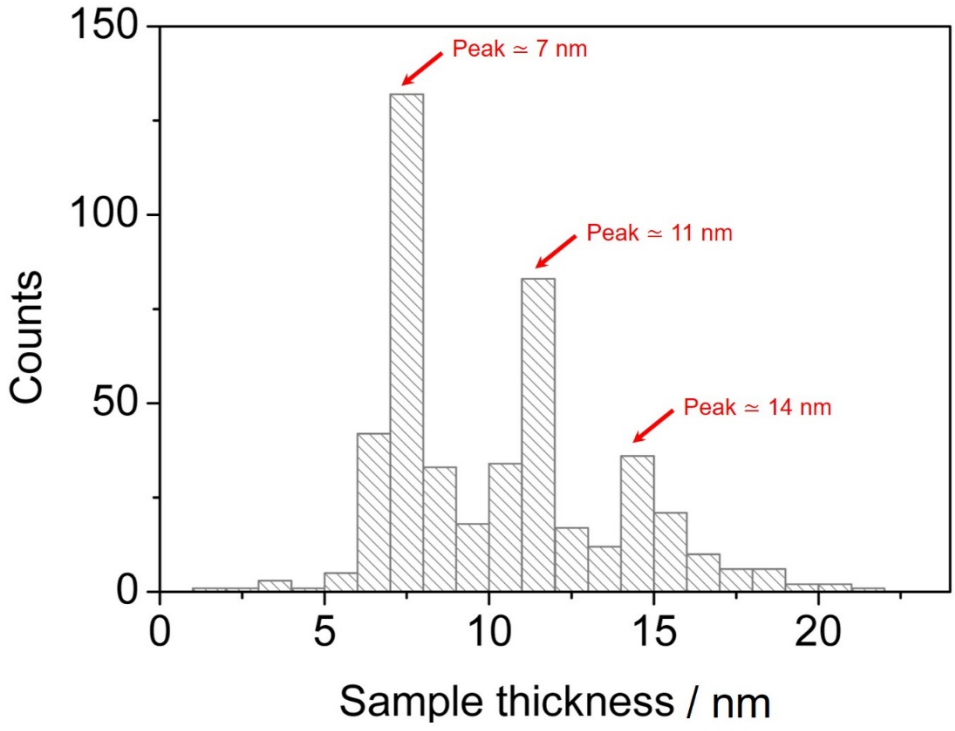

Figure S12. Sample thickness histogram showing the heights related with all the force-distance curves taken onto the GSL SLM in 10 mM HEPES, 300 mM NaCl and 20 mM $MgCl_2$ (pH=7.4). Three main peaks at about 7 nm, 11 nm and 14 nm are clearly visible.

5e) 3-layer regions nanomechanical analysis

The nanomechanical analysis reported in the manuscript (Figure 3) was performed on 2-layer and 4-layer regions. Only these patches, indeed, can be considered equivalent from the elastic point of view since they expose to the indenting tip the same molecular region, *i.e.* the polar heads.

For the sake of completeness, the same nanomechanical analysis was performed also on 3-layer regions (*ca.* 11 nm thick, see Figure S12), exposing their hydrophobic tails to the liquid environment. In Table S1, all the Young modulus values, for every thickness and contact mechanics model, are reported. For Sneddon's model, the 3-layer data follows the same trend as the 2-layer and 4-layer thick regions, *i.e.* the thicker the indented layer, the less relevant the bottom-effect artefact and, therefore, the smaller the

elastic modulus value. Notably, for Garcia's 4th order correction, a change of this trend is observed, at least in the mean Young modulus value with 3-layer regions showing the lowest elastic modulus. This could be due to an indented slightly softer region, made up of hydrocarbon chains and not polar heads. Unfortunately, the error bars do not allow us to push forward this observation whose rationalization is beyond the scope of this contribution.

	SNEDDON [MPa]	**GARCIA, 1st ORDER [MPa]**	**GARCIA, 4th ORDER [MPa]**
2-layer	360 ± 11	214 ± 7	134 ± 5
3-layer	239 ± 11	154 ± 7	123 ± 10
4-layer	229 ± 11	156 ± 8	125 ± 7

Table S1. Young moduli values for regions 2-layer, 3-layer and 4-layer thick. The second column shows the elastic moduli obtained with Sneddon's contact mechanics model where no bottom-effect correction is considered. The third column reports the elastic moduli obtained with Garcia's formula (Equation 3) truncated at the 1st order. The fourth column reports the Young moduli obtained with Garcia's formula (Equation 3) truncated at the 4th order.

5f) χ^2 threshold

The selection of the relevant force-distance curves was done selecting an appropriate χ^2 threshold. The whole number of pixels in a force-distance curve was 1024 therefore providing about 70 pixels for each force-indentation curve which had a max indentation of *ca.* 1 nm in order to support the hypothesis of a paraboloidal tip geometry

and a linear nanomechanical response of the sample, see Figure 2c. Following standard statistics, the χ^2 threshold was selected to be ten, about one order of magnitude smaller than the number of available pixels (n = 70), therefore fulfilling the requirement of a high fit goodness (χ^2 < n) but maintaining at the same time a significant number of events.

6. AFM tip radius measurement

The measurement of the tip radius *R* is critical for a correct calculation of the Young modulus of the sample. Several methods have been proposed in the literature,[9] among them, in this contribution, a reference sample with a known Young modulus was scanned plus a Scanning Electron Microscope (SEM) image of the AFM tip will be provided in Section 7. Specifically, a 1.5 x 1.5 μm^2 image of a commercial polystyrene and polyolefin elastomer (ethylene-octene copolymer) PS-LDPE test sample (Bruker), before and after the official experiment, was scanned in Peak-Force AFM. The elastic modulus vales of these two materials are known to be about 2 GPa and 100 MPa, respectively.

In Figure S13a, the topography of an LDPE circular domain embedded in a PS matrix, imaged before the official experiment, is clearly visible. From the stiffness channel provided by the Peak Force technique (Figure S13b), it was then possible to extrapolate the mean *effective* Young modulus (see the histogram reported in Figure S13c) of the central region of the circular domain. Setting a tip radius R = 15 nm we were able to tune this mean value to about 130 MPa, the proper *effective* elastic modulus necessary to provide a *sample* Young modulus of 100 MPa, see Equation 2 of the main text. Nominally the tip radius of a SCANASYST FLUID + cantilever (Bruker) should be smaller than 12 nm, therefore we considered R = 15 nm still acceptable, maybe bigger due to small contaminations arising from the scanning of the test sample.

The same procedure was repeated at the end of the experiment, resulting in a higher tip radius of 19 nm (Figure S13d-e-f). We therefore selected a tip radius R = 17 nm (average value between 15 and 19 nm) as the value for the nanomechanical analysis (Figure 3) and the finite element method (FEM) simulations (Figure 4).

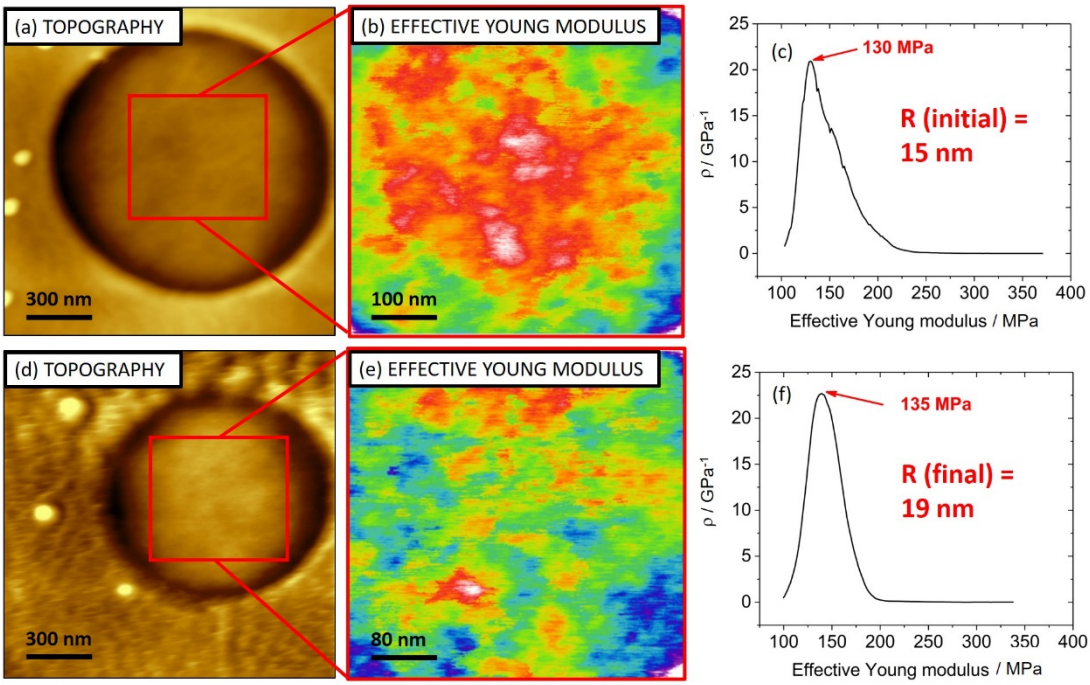

Figure S13. Peak Force images (topography and effective stiffness) of a PS-LDPE test sample (Bruker), before (a-b) and after (d-e) the official experiment. a,d) Topography image showing an LDPE circular domain embedded in a PS matrix. b,e) Effective stiffness of the central part of the circular domains shown in Figure S13a-d. c) Effective stiffness histogram relative to Figure S13b showing a pixel distribution (ρ) with a mean value of 130 MPa. f) Effective stiffness histogram relative to Figure S13e showing a pixel distribution (ρ) with a mean value of 135 MPa.

Finally, in order to demonstrate the robustness of Garcia's bottom-effect correction with respect to a tip radius of 17 nm whose error bar is not well known, the Nanomechanics Python code for different values of R, from 13 nm to 25 nm, was run.

Figure S14 shows the evolution of *delta*, *i.e.* the difference between the average sample Young modulus of 2-layer and 4-layer data, with respect to the aforementioned tip

radius values. A perfectly compensated bottom-effect artefact should provide a *delta* value equal to 0.

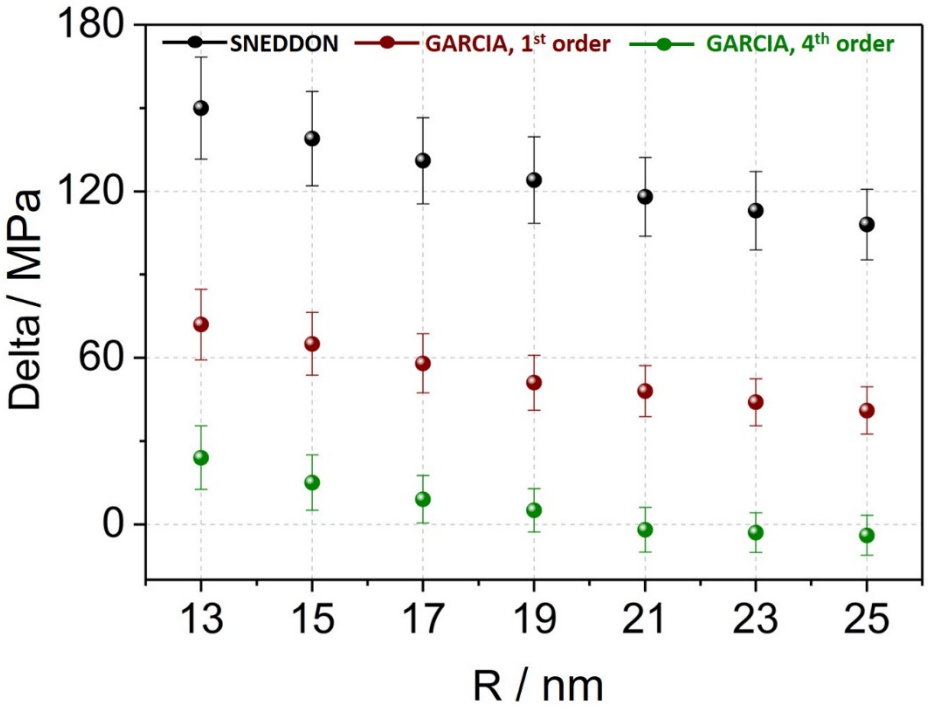

Figure S14. Effect of the tip radius on the bottom-effect artefact correction for Sneddon's model (black data), Garcia's theory at the 1st order correction (dark red data) and Garcia's model at the 4th order correction (green data). The main parameters used in the simulation are: k = 0.6878 $N \cdot m^{-1}$, deflection sensitivity S = 14.46 $nm \cdot V^{-1}$ (for the calibration of the last two values see the AFM methods Section), χ^2 = 10, tip geometry: paraboloidal.

In the range of tip radius values considered in Figure S14, Sneddon's equation is never providing a *delta* value close to zero, *i.e.* this contact mechanics model is not able to compensate the bottom-effect artefact, independently of the tip radius. When Garcia's 1st order correction is considered, instead, the *delta* value decreases significantly while the 4th order correction basically results in *delta* values close to zero for all the tip radius values between 13 nm and 25 nm. Indeed, in this tip radius range, an average delta value of (9 ± 5) MPa is obtained. Hence, it can be concluded that Garcia's 4th order correction compensates the bottom-effect artefact independently of the tip radius. As a

final observation, for tip radius smaller than 17 nm, even Garcia's 4th order *delta* values are slightly different from zero. Eventually, a full compensation could be reached considering viscoelastic effects or maybe passing to the 5th order bottom-effect artefact correction (whose analytical expression is not yet reported in the literature).

7. SEM tip shape and radius

As a second method to measure the tip radius and also to determine its shape, a Scanning Electron Microscope (SEM) experiment was done. In Figure S15a the cantilever is clearly visible together with the associated tip. In Figures S15b and S15c, two magnified images of the tip are provided: from here a tip radius R = 16 nm was measured. Notably, this value agrees with the tip radius obtained in Section 6 (see Figure S13).

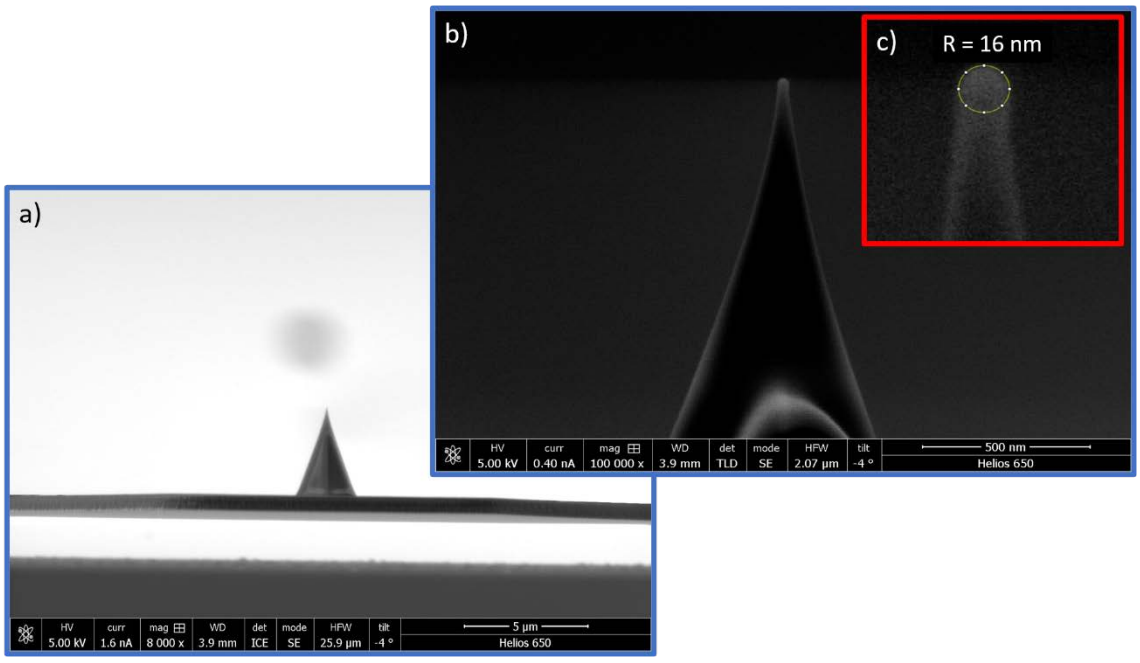

Figure S15. a) SEM image of the cantilever+tip system. b) SEM magnified image of the tip. c) SEM magnified image showing only the apex. The calculated tip radius is R = 16 nm.

8. Additional force-distance curves for Figure 2b

To confirm the trend described in Figure 2b, Figure S15 shows ten additional force-Z(piezo) curves where basically the same breakthrough-shape can be noticed, with a mean breakthrough force at around 20 nN as reported in Figure S9.

Additionally, no negative forces can be observed for each and every force curve, therefore confirming, as required by the Sneddon model (see Figure S8), that no adhesion occurs in the tip-sample interaction.

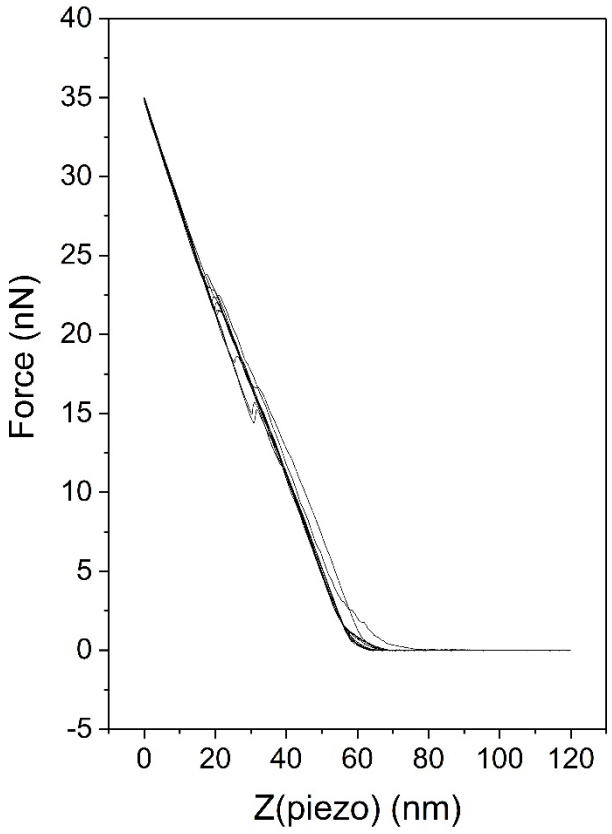

Figure S16. Ten force – Z(piezo) experimental curves exhibiting the same shape as the one shown in Figure 2b of the main manuscript. Furthermore, no adhesion can be observed.

References

1. Doepner, A. M.; Aboagye, E. O.; Barrett, A. G. M., *TETRAHEDRON LETTERS* **2015,** *56*, 3293-3297.
2. Garcia-Manyes, S.; Sanz, F., *Biochimica et Biophysica Acta (BBA) - Biomembranes* **2010,** *1798* (4), 741-749.
3. Gavara, N., *Scientific Reports* **2016,** *6*, 21267-21280.
4. Voïtchovsky, K.; Antoranz Contera, S.; Kamihira, M.; Watts, A.; Ryan, J. F., *Biophysical journal* **2006,** *90* (6), 2075-2085. DOI 10.1529/biophysj.105.072405.
5. Butt, H.-J.; Cappella, B.; Kappl, M., *Surface Science Reports* **2005,** *59*, 1-152.
6. Garcia-Manyes, S.; Redondo-Morata, L.; Oncins, G.; Sanz, F., *Journal of the American Chemical Society* **2010,** *132* (37), 12874-12886.
7. Müller, D. J.; Engel, A., *Biophysical journal* **1997,** *73* (3), 1633-1644.
8. Prinetti, A.; Loberto, N.; Chigorno, V.; Sonnino, S., *Biochimica et Biophysica Acta (BBA) - Biomembranes* **2009,** *1788* (1), 184-193.
9. Santos, S.; Guang, L.; Souier, T.; Gadelrab, K.; Chiesa, M.; Thomson, N. H., *Review of Scientific Instruments* **2012,** *83* (4), 043707.